XENON HYPERPOLARISED GAS GENERATOR

FOR

FUNCTIONAL LUNG MRI

By

Maryam Arianpouya

A THESIS SUBMITTED TO MACQUARIE UNIVERSITY

FOR THE DEGREE OF MASTER OF RESEARCH

DEPARTMENT OF ENGINEERING

APRIL 2017

Sydney ~ Australia

Except where acknowledged in the customary manner, the material presented in this thesis is, to the best of my knowledge, original and has not been submitted in whole or part for a degree in any university.

_____

Maryam Arianpouya

Dedication

To my Family,

For always believing in me.

Acknowledgements

First and foremost, I would like to express my deep sense of gratitude to my supervisor, Dr. Yves De Deene for his help and support throughout this project. Lessons that he taught me are invaluable and will be with me wherever I go.

I would also like to thank Dr. John De Poorter for his insight and guidance along the way, believe me, to know him is to never forget him.

I wish to acknowledge Macquarie University for awarding me the international Research Training Pathway (iRTP) scholarship. Without it this journey was not possible.

Abstract

Conventional Magnetic Resonance Imaging (MRI) has superior soft tissue contrast but limited potential in imaging low-density lung tissue and molecular tracer because of the relatively low intrinsic sensitivity. In this project, we focus on increasing the sensitivity with several orders of magnitude using hyperpolarised ^{129}Xe (hp-^{129}Xe) MRI. A small scale hyperpolarised ^{129}Xe gas generator is currently under construction in house in Macquarie University. The system has further been developed and optimized through this Master of Research project (MRES). Improvements in hardware have been achieved on the NMR unit and the gas-vapour flow system. The improved NMR unit is able to detect polarisation as low as 10%. The gas-vapour flow system was optimized through a new design in the optical pumping cell and reducing gas leakage. Calibrations were performed to find the most optimum parameters to run the polariser. A protocol was presented for operating the polariser with the optimized parameters. A Matlab program was also further developed to control transmit-receive NMR process. The system will be able to polarise sufficient amounts of ^{129}Xe gas for phantom and preclinical MRI experiments in small rodents (post-MRES). The focus of these experiments will be on pulmonary functional imaging.

Contents

List of Figures

List of Tables

1

Introduction

Magnetic Resonance Imaging (MRI) is a powerful and most versatile diagnostic imaging technology that has been around since eighteen. Conventional MRI has predominantly been used to image tissues with a high density of ^{1}H protons for reasons of sensitivity (Fig.1.1). The sensitivity is proportional to the population difference between two nuclear spin energy eigenstates as shown in Figure 1.2b. MRI of low-density lung tissue and molecular (tracer) imaging with conventional proton-based MRI has so far been very limited because of the relatively low sensitivity of proton MRI as compared to nuclear imaging techniques using radioactive isotopes. In recent years, in an attempt to increase the sensitivity with several orders of magnitude, hyperpolarised MRI techniques using noble gases (^{3}He and ^{129}Xe) have been proposed.

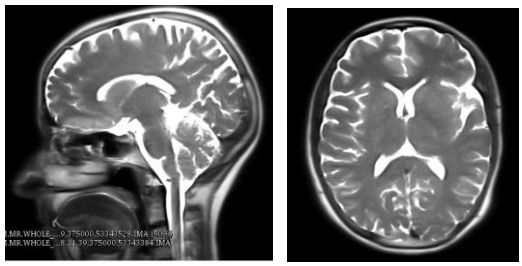

Figure 1.1. High contrast MRI image of the author's brain scanned on a 3T Siemens MRI scanner at Macquarie University Hospital (MUH).

The first hyperpolarised-gas MRI images with hyperpolarised ^{129}Xe (hp-^{129}Xe) were acquired at Stony Brook/ Princeton in 1994 [1], and hp-^{129}Xe images of the human lung were obtained a few years later [2]. However, until now, most of the research on hp-gas MRI has been focused on ^{3}He because of two major favourable physical properties; its relatively large gyromagnetic ratio and higher achievable polarisability. However, ^{3}He is becoming increasingly limited because of its limited availability and related high cost ($2000/Litre in 2010) [3]. As a result, insufficient ^{3}He is currently a great concern to translate hyperpolarised ^{3}He MRI from research into clinical practice. The other noble gas, ^{129}Xe, however, has a higher availability as it can be extracted from the air. Currently, isotopically-enriched xenon gas (~80% ^{129}Xe) can be purchased for about $100/Litre [2]. ^{129}Xe also exhibits other favourable properties such as a high solubility in blood which enables it to be used as a tracer [4]. In addition, ^{129}Xe can be encapsulated in a molecular cage which creates potential in molecular imaging. These substantial features now place hp-^{129}Xe MRI on a brighter future for

preclinical and clinical imaging. However, ^{129}Xe is more challenging to polarise [5]. While ^{3}He historically had a polarisation level higher than 30% for litre-quantities, polarisation levels for similar quantities of pressurized ^{129}Xe have been in the order of 10% [3]. Since the MRI signal-to-noise ratio (SNR) is directly proportional to the amount of polarised ^{129}Xe, it is sensible to develop novel methods to achieve higher polarisation levels.

1.1 Motivation for Research

1.1.1 Hyperpolarised Versus Thermal Gas Imaging

The use of MRI for pulmonary imaging based on the conventional method has been significantly limited by at least 3 major obstacles [3]: Firstly, the concentration of hydrogen protons (^{1}H) in lung tissue relative to other soft tissues is only one-third that of human tissue with a mass density close to unity which results in inherently low nuclear magnetic resonance (NMR) receptivity of lung tissues. Secondly, magnetic field inhomogeneities as a result of magnetic susceptibility differences between air and lung parenchyma will result in short MRI relaxation times which makes imaging cumbersome. Thirdly, macroscopic movements of cardiac and respiratory organs and blood flow also compromise the image quality. Although recently, some innovative imaging techniques such as ultrashort echo time (UTE) MRI have some promising features [3], conventional ^{1}H MRI has been found inapplicable for imaging of the lung airspaces.

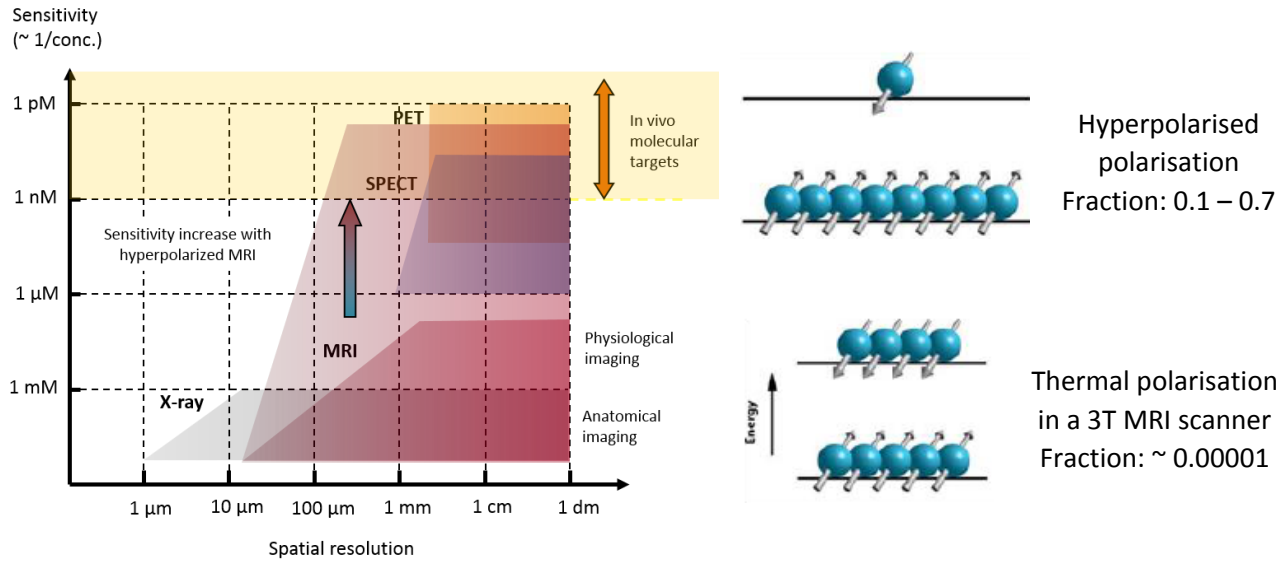

(a) **(b)**

Figure 1.2. Typical range of imaging receptivity, expressed in detectable concentrations and spatial resolution of different medical imaging modalities [3] (a). Conventional MRI has a high spatial resolution but a relativity poor sensitivity due to the small population difference between the Zeeman nuclear spin energy states (b-bottom). Using hp-noble gas (b – top) a much higher population difference can be obtained. The increased sensitivity with hyperpolarised gas brings MRI in the range of radionuclide imaging technologies (a).

The use of optically polarised noble gas isotopes (^{3}He and ^{129}Xe) as imaging agents enables imaging of air cavities such as the bronchial tree and lungs. In addition, dynamic functional images of lung ventilation can be obtained with hyperpolarised gas MRI.

The signal strength in conventional MRI is proportional to the population difference of quantum eigenstates as described by the Boltzmann equation: $\frac{N_{\uparrow}}{N_{\downarrow}} = e^{-\frac{\Delta E}{kT}} = e^{-\frac{\gamma \hbar B}{kT}}$ where ΔE is the energy difference between the Zeeman energy eigenstates, k is the Boltzmann constant ($k = 1.38\ 10^{-23} m^2\ kg\ s^{-2} K^{-1}$), T is the absolute temperature, γ is the gyromagnetic constant and $\hbar$ is the reduced Planck constant ($\hbar = \frac{h}{2\pi} = 1.054\ J\ s$). In a 3T MRI scanner, the population difference between the quantum energy eigenstates amounts to 0.00001. With hyperpolarisation, an increase in nuclear magnetization by roughly 10,000 times can be achieved [3]. Therefore, hyperpolarisation makes MRI competitive with nuclear imaging methods employing radionuclides for molecular imaging (PET and SPECT) (Fig.1.2a).

1.1.2 Functional Lung Imaging and Hp-^{129}Xe Imaging Potential

Various functional lung imaging studies have been conducted. Functional Dual-Energy CT (DECT) imaging is based on the different absorption of X-rays at two different energies by Iodine-based contrast media or inhaled xenon gas. DECT provides high-resolution quantitative imaging of perfusion-ventilation of the lung. However, exposure to ionizing radiation has substantially limited this technique to gain widespread acceptance. Other methods are based on functional radionuclide imaging [6]. Scintigraphy and Single Photon Emission Computerized Tomography (SPECT) have been applied to acquire quantitative ventilation maps from obstructive lung diseases by radioactive gases such as ^{133}Xe, ^{127}Xe, ^{81m}Kr or radioactive aerosols such as ^{99m}Tc-DTPA. Lung perfusion maps can be obtained by injecting radioactive ^{99m}Tc labeled albumin. In addition, PET imaging with 18F-fluorodeoxyglucose (FDG) has been successfully applied for ventilation-perfusion of both human and animal lungs. FDG-PET is currently combined with CT for mapping the functional information onto the anatomical CT image. However, it is important to note that all these techniques have a substantial well documented risks of exposing patient to nuclear radiation, suffer from a significant poor spatial and temporal resolution, and provide limited structural information. In contrast, hyperpolarised noble gas MRI is a safe imaging technique, using only radiofrequency electromagnetic waves and static magnetic fields to provide high-resolution images. Hp-^{3}He MRI has been thoroughly explored to quantify different functional properties of the lung [7-11]. Recent studies have indicated the potential of hp-^{129}Xe in quantitative imaging of static and dynamic ventilation, alveolar microstructure (using gas diffusion measurements) and partial oxygen concentration [12-14].

- ***Ventilation, gas diffusion and gas exchange:*** When air is inhaled and arrives in the alveoli, oxygen is taken up by the blood capillaries and CO_2 is excreted from the blood capillaries into the alveoli. Subsequently, the CO_2 rich gas is exhaled. The process of O_2–CO_2 gas exchange in the alveolar sacs is related to several factors such as the blood perfusion in the blood capillaries, the state of the lung parenchyma and mucosa. Many obstructive lung diseases, including emphysema, asthma, and cystic fibrosis, exhibit disturbed gas exchange (Fig.1.3). Detecting the early onset of pulmonary obstructive disease, monitoring the progression of gas exchange abnormalities and follow up of pharmacological interventions require quantitative methods that provide regional information. During a static ventilation scan, the tracer (hp-^{129}Xe) gas is inhaled by the patient and a fast MRI scan is taken to image the distribution of the gas in the lung, typically using low-flip-angle gradient-echo (GRE) pulse sequence. The gas distribution can also be scanned dynamically during inhalation and exhalation. This method shows a high potential of the hp-gas MRI in showing the lung physiology that have never been possible before with other functional imaging modalities.

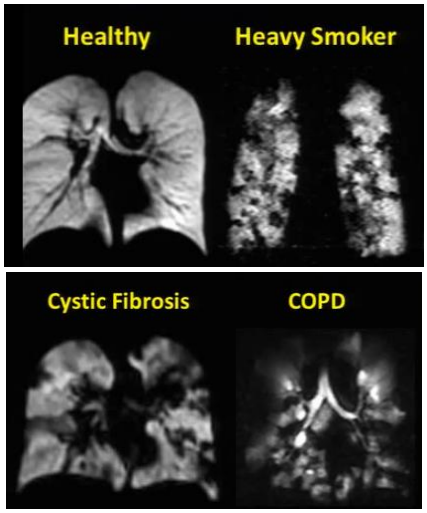

Figure 1.3. hp-^{3}He is uniformly distributed in a healthy lung. In contrast, defects are observed in diseased lungs corresponding to areas of lung not ventilated or poorly ventilated within a typical 8–16 s breath-hold scan [15-16].

- ***Alveolar microstructure:*** The lungs have a typical fractal structure. It has approximately 24 generations of branching with a wide range of diameters from 20 mm in the trachea down to a few hundred microns in the alveoli (Fig.1.4). As a result of these small cavities, the molecular displacement of the gas molecules is hindered. MRI diffusion measurements obtained with different diffusion times can be used to assess the microstructure of the lung tissue. Computational modelling of restricted diffusion can help in correlating the MRI diffusion weighted signal with the alveolar microstructure.

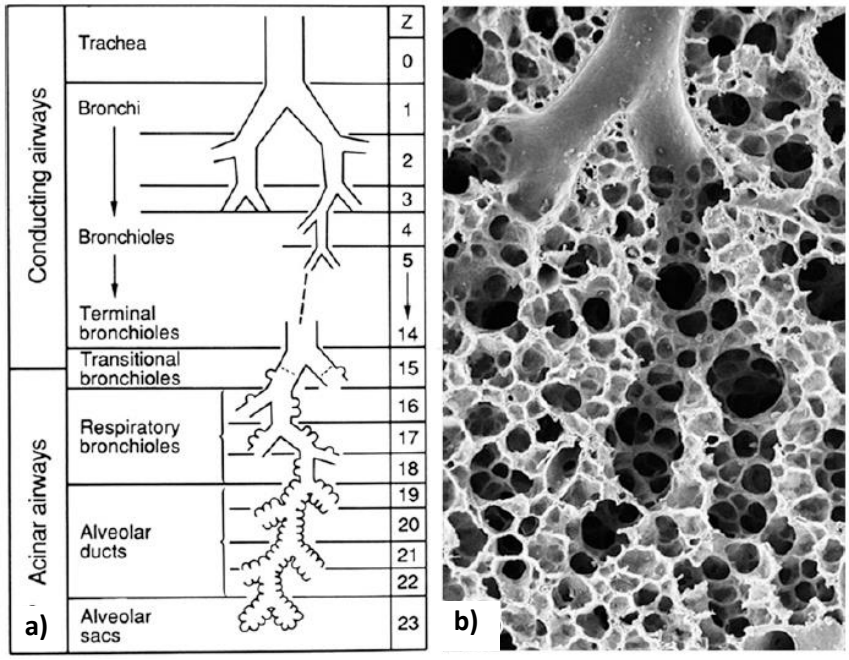

Figure 1.4. Weibel's model of branching airways of the lung (a) with surface complexity occurring in the last eight generations (b) [17].

- ***Partial oxygen concentration in the lung:*** Pure hyperpolarised noble gases have relaxation times much longer than those found in biological tissues. In the lung, the longitudinal relaxation time (T_1) of the gas is substantially reduced. The longitudinal relaxation rate ($1/T_1$) of noble gases is directly proportional to the concentration of oxygen [18-20]. This relationship can be exploited to map pO_2 in the lungs.

1.1.3 Molecular Imaging Using Hyperpolarised Gas MRI

Cancer, neurological and cardiovascular disease treatments are being progressively shifted from conventional chemotherapy toward molecular targeted therapies. Molecular imaging modalities which have a high sensitivity to detect exogenous tracers are able to substantially contribute to this approach. Among all imaging techniques, MRI, radionuclide imaging including Positron Emission Tomography (PET), Single Photon Emission Computed Tomography (SPECT), and fluorescent optical imaging have a significant potential to move beyond conventional structural imaging. However, conventional MRI has lagged behind radionuclide or fluorescence imaging due to its lower intrinsic sensitivity. While radionuclide-based methods are able to detect concentrations of radiotracers in the range of 10^{-11} to 10^{-12} mol/L for PET and 10^{-9} mol/L for SPECT [21], conventional MRI can only detect tracers with concentrations of about 10^{-3} to 10^{-5} mol/L [22]. In an attempt to increase the sensitivity of MRI, macromolecular reporter molecules with increased T_1 or T_2 relaxivity have been designed. However, these molecular tracers are too large to permeate the blood vessel wall. Recently, hyperpolarised ^{129}Xe has been proposed as a biomolecular probe because of its two major favourable physical properties: it has a high solubility which can enter the bloodstream and circulate within the entire body. Also, it shows a large chemical shift which strongly depends on the molecular environment. This probe combines hyperpolarisation and chemical exchange saturation transfer to create a signal enhancement of in the order of 10^8 – 10^9 and is referred to HyperCEST (Fig.1.5). This novel method has great potential for molecular MR imaging.

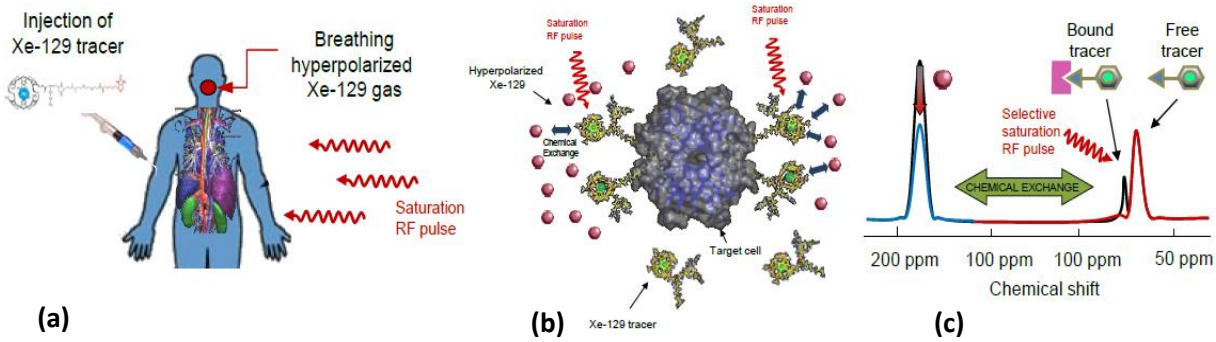

Figure 1.5. HyperCEST combines hyperpolarisation and chemical exchange saturation transfer [23]. ^{129}Xe encapsulated by a molecular tracer is injected into the patient. After distribution of the tracer to the target cells, hp-Xe gas is administered by inhalation (a). The encapsulated ^{129}Xe in the tracer, the free hp-Xe and the bound ^{129}Xe tracer have distinct resonance peaks (c). Chemical exchange between the different Xenon pools enables the use of chemical exchange saturation transfer (CEST) MRI to visualize the presence of bound tracer molecules (b).

1.2 Hyperpolarised Gas Generator in Principle

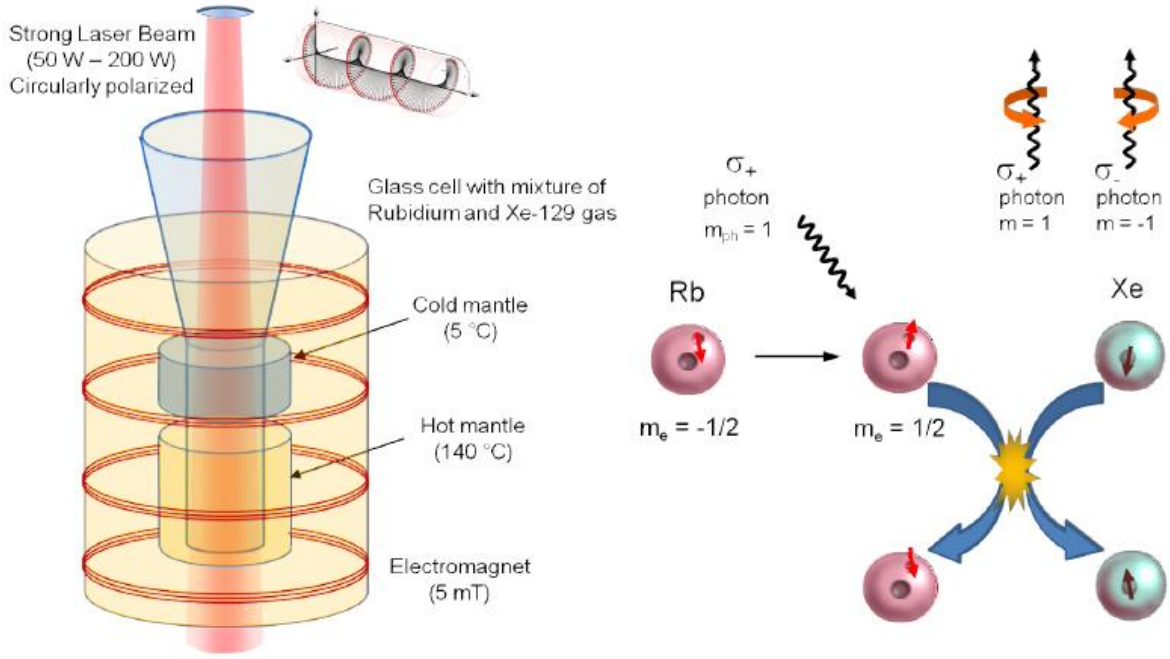

Figure 1.6. Principle of hyperpolarisation of gases by use of spin exchange optical pumping (SEOP) [24].

Compared to the requirements for routine proton MRI, several additional considerations are required to conduct hyperpolarised MRI. First and foremost is preparing the noble gas in the hyperpolarised state before it can be inhaled by the patient. The gas polarisation principle is based on the method of "Spin-Exchange via Optical Pumping" (SEOP) [24]. The principle of SEOP was demonstrated by Kastler in the early 1950s, many years before being applied to medical imaging. SEOP contains two major steps: the first step is optical pumping which involves magnetic polarisation of the valence electron of an alkali metal, e.g. Rubidium (Rb), by use of a circularly-polarised beam of laser light at the wavelength corresponding with the excitation level. In the second step, the magnetic polarisation of Rb electrons is transferred to the noble-gas nuclei (^{129}Xe or ^{3}He) through atomic collisions. Two buffer gases, Nitrogen (N_2) and helium (^{4}He), facilitate polarisation transfer to the noble gas nucleus. N_2 acts as a quenching gas to suppress the Rb excited fluorescence states. ^{4}He is added for 'pressure broadening' of the Rb spectral absorption of the laser light. Figure-1.6 shows a schematic of the principle of SEOP method.

This method is conducted in a system, a so-called 'polarisation generator', which can operate in either a 'batch' mode or continuous flow mode. The batch method is based on polarising batches of noble gas in an isolated pumping cell which is regularly filled with a fresh gas mixture. In the continuous-flow mode, the gas mixture flows continuously through the optical cell during the polarisation process.

1.3 ^{129}Xe Properties and Polarisation

Of the nine stable isotopes of xenon, ^{129}Xe has a nuclear spin of ½ which can be detected by MRI. It is an inert gas that can be inhaled or injected into the subject in the form of emulsions. No adverse health side effects have been reported [3]. ^{129}Xe has a low diffusion coefficient (~0.06 cm^2/s @ 1 atm, 20°C) and a relatively low gyromagnetic ratio (-11.78 MHz/T). These two features together decrease spin dephasing due to off-resonance effects as a result of magnetic-susceptibility differences [3]. Less spin dephasing will eventually result in less signal attenuation. ^{129}Xe also has a very high solubility coefficient in a variety of substances (water: 0.083 and blood: 0.14). Dissolved ^{129}Xe in the blood plasma, the lung parenchyma and red blood cells exhibits specific large spectral shifts which makes hp-Xe a potentially valuable probe for studying gas exchange between the alveolar space and parenchyma and gas uptake in the lung [3]. Also, the ability of ^{129}Xe to enter the bloodstream and to circulate within the entire body potentially facilitates the use of hp-Xe imaging elsewhere such as for the brain and abdominal organs [25-26].

Polarised ^{129}Xe on a small scale is provided in the batch mode polariser via SEOP method. Once the Rb valence electron is polarised, the polarisation is expected to transfer to ^{129}Xe nucleus in a few seconds via sudden binary collisions or long-lived ^{129}Xe-Rb van der Waals interactions. However, polarisation typically takes several minutes (5-20 min) [27]. This occurs mainly because a rubidium atom is highly interactive with other Rb atoms forming nano-clusters. Nano-clusters are formed from several Rb atoms (n = 3, 19, 29, …) [28] during operation causing Rb depolarisation. This significantly reduces the ultimate achievable ^{129}Xe polarisation degree, and the polarisation rate. In order to overcome this limitation, a "flow-through" hyperpolarised cell was developed by Driehuys et al. [29]. In this system, a mixture of gases with a low fraction of ^{129}Xe (typically ~1%) flow continuously through the optical cell. ^{129}Xe atoms pass through the cell in a time span of only a few seconds. This approach has two substantial advantages over the batch mode: Firstly, the low concentration of ^{129}Xe restricts Rb electron-spin destruction collisions. Secondly, the overall polarisation time of the xenon atoms is significantly decreased. As a result, larger gas quantities are obtained via continuous-flow mode polarisers in a shorter time.

Most of the initial research on ^{129}Xe SEOP processes were done on a small scale. The first SEOP hyperpolarised xenon was presented by B.C. Grover in 1978 [30]. He measured 10% of hyperpolarisation of ^{129}Xe using a small amount of xenon gas, 0.6 mbar of 65% enriched xenon in a 15 cc spherical closed cell. To date, the highest amount of polarisation produced in the batch mode has been 70% reported by the Marburg group using a 2 W Ti: Sapphire laser.

For continuous flow mode polarisation method, a significant polarisation amount was obtained by Ruset and co-workers [31] at the University of New Hampshire. He introduced a massive polariser (with a large optical cell of ~1.8 m length), and optimized the continuous flow design system which

was able to deliver 50% hyperpolarised ^{129}Xe with the production rates of 1.2 L/hr. Recently the group of Clifford Bowers [32] from the University of Florida was able to polarise ^{129}Xe over 65% with the novel design in geometry for the cell and seven coherent 210W diode lasers. Several studies were done on Xenon polarisation dependencies on different operational parameters of batch and continuous-flow mode systems such as total pressure, gas mixture, and laser power. The results are presented in Table 1.2, and will be used for comparison with our work once hyperpolarised ^{129}Xe gas is achieved.

Group [ref]	Gas Mixture	Laser Power (W)	Pressure (atm)	β_{129} (%)	^{129}Xe Flow (cm^3/min @ 1 atm. & 0 °C)	Polarisation (%)
Batch System						
Berkeley [33]	100%Xe	0.03	0.8	70	-	0.5
Michigan [34]	92%Xe+8%N_2	30	2.2	26.4	-	7.5
Nottingham [35]	40%Xe+60%N_2	23.3	0.5	85	-	14
Vanderbilt [36]	16%Xe+84%N_2	200	2.6	26.4	-	30
Osaka [37]	5%Xe+95%N_2	90	0.15	26.4	-	63.6
Marburg [38]	2%Xe+98%N_2	2	0.1	26.4	-	70
Continuous Flow System						
Princeton [29]	1%Xe+1%N_2+98 %He	50	10	71	6	5
Princeton [39]	1%Xe+1%N_2+98 %He	100	10	71	3.2	20
Washington [40]	1%Xe+1%N_2+98 %He	40	7	26.4	0.6	10
Marburg [38]	2%Xe+98%N_2	2	0.1	26.4	0.1-0.8	20
Michigan [34]	92%Xe+8%N_2	30	2.4	26.4	8.3	7.5
New Hampshire [31]	1%Xe+1%N_2 +98%He	90	0.65	86	1360	50
Florida [41]	1%Xe+1%N_2 +98%He	7 × 210	3	86	2.45	65

Table 1.1. ^{129}Xe polarisation results obtained by different research groups, (β_{129}: the xenon enrichment factor)

Based on these research, the polarisation seems to increase by going from moderate to low total pressures, mainly because Rb-Xe long-lived van der Walls interactions are dominant at low pressures which will result in more efficient spin-exchange. The laser power dependence showed a saturation of the polarisation after a certain level. Lower ^{129}Xe densities in the mixture leads to higher polarisation due to higher ^{129}Xe spin polarisation and lower Rb electron-spin destruction. Research also show that polarisation has a high dependency on the cell geometry (surface/volume) specifically

at low pressures [31]. The reason for this is found in the dependency of Rubidium spin-destruction rate on Rubidium interactions with the cell wall. Wall coatings have been proposed to overcome high Rubidium spin-destruction rate [42]. Coatings are typically silicone based such as Dry-Film, octadecyldimethylchlorosilane, and Surfasil.

As a conclusion of these studies one would expect the highest polarisation to occur for a low concentration of xenon, a moderate laser power, and a low pressure with a coated SEOP cell surface.

1.4 Research Framework and Objectives

This project is defined in five major phases. First and foremost is the preparation of hyperpolarised ^{129}Xe gas on a small scale polariser. The batch mode gas polariser is currently under construction in house in Macquarie University (MU polariser). The MU polariser has further been developed and optimized through this Master of Research project (MRES). This system will be able to polarise sufficient amounts of ^{129}Xe gas for phantom and preclinical MRI experiments in small rodents at the end of this phase. These experiments will be performed at the preclinical MRI facility of the University of New South Wales (UNSW) in a second phase (post-MRES). The focus of these experiments will be on the acquisition of quantitative maps of regional ventilation, gas diffusion, gas exchange, alveolar size distribution and local oxygen pressure on the pulmonary system of small animals.

A large-scale continuous-flow hyperpolarised gas polariser is also under construction in Macquarie University. In the third phase of the project, this system will be further developed and optimized. This system will be able to hyperpolarise larger gas volumes with a sufficient degree of polarisation that will allow human lung imaging in the fourth phase of the project. The hp-gas will be applied for physiological human lung studies at the clinical 3T MRI scanner of Macquarie University Hospital (MUH) which has been recently equipped by the Macquarie University research team with a broadband transmit system. In the fifth phase, further research will focus on using hp-^{129}Xe for molecular imaging.

This nine-month MRES project was started in July 2016 to satisfy the first phase of this project. The main objectives of this research work are outlined as follow:

I. To further develop the MU gas polariser. The majority of the construction was already done before starting this MRES project. However, some issues still remained mainly in the gas-vapour flow system, the NMR hardware, and the user interface.
II. To obtain the most optimum operational parameters of the polariser related to the laser, gas-vapour flow system, NMR instrumentation and heating apparatus.
III. To investigate an operational instruction for running the polariser.

1.5 Thesis Overview and Contributions

This thesis consists of five chapters as follow:

- Chapter 1, *Introduction*, includes this introduction which reviews the hyperpolarised gas capabilities and applications, polarisation principle and background, and the research framework.
- Chapter 2, *Theoretical Background*, describes the necessary theoretical background for Rb optical pumping and spin transfer to ^{129}Xe. The relevant NMR methods are also briefly reviewed in this chapter.
- Chapter 3, *Instrumentation and Experimental Setup*, provides an overview of the MU ^{129}Xe gas polariser.
- Chapter 4, *Results and Discussions*, contains our main experimental results followed by a detailed discussion. New Design and Improvements in the polariser hardware are presented. Optimum experimental parameters of the polariser were found and are discussed. The running protocol for operating the polariser is presented.
- Chapter 5, *Conclusions and Future Work*, summarizes the acquired results and underlines its relevance and implications on our planned future work.

The results of this work have been presented in:

- Maryam Arianpouya, Yves De Deene, "*Functional Lung Imaging Using Hyperpolarised Xenon-129*" (Oral Presentation in MedPhys 2016 on 8th December 2016 at Sydney University (Dec 2016)

2

Theoretical Background

Hyperpolarisation provides a nuclear magnetization that is several orders of magnitude higher than the thermal magnetization. The nuclei of noble gas atoms are magnetized via Spin Exchange Optical Pumping (SEOP) in a hyperpolarised gas polariser. Noble gas atoms have a full valence shell allowing spin polarisation to be transferred directly to the nucleus. He-3 and Xe-129 isotopes have been typically used over other noble gas nuclei in medical imaging [43]. In particular, Xe-129 has unique properties considering its potential in molecular MR imaging, as discussed in Section 1.1.3.

SEOP is a two-step process, as discussed in Section 1.2: optical pumping and spin-exchange. This chapter provides a theoretical overview of these two steps and discusses the key points in polarisation of noble gases. In addition, the basic principles of NMR for polarisation detection will be presented.

2.1 Optical Pumping

Optical pumping is based on the polarisation of valence electron of alkali metals, which occurs through resonant absorption of circularly polarised laser beam tuned to the D1 transition energy [44]. The D1 transition is from the electronic ground state of $^2s_{1/2}$ to the excited state of $^2p_{1/2}$. The most common alkali metal used in optical pumping experiments is Rubidium because of its two favourable properties: Firstly, it has a low melting point of 39°C leading to a high vapour density in the order of 10^{12}-10^{15} cm^{-3} at temperatures between 80-200°C. Rubidium vapour density can be calculated from the equation [45]:

$$[Rb] = \frac{10^{10.55-4132/T}}{1.38\times10^{-16}T}\ (mol/cm^{-3}) \tag{2.1}$$

where T is the equilibrium absolute temperature. A plot of this relationship is also shown in the Fig.2.1.

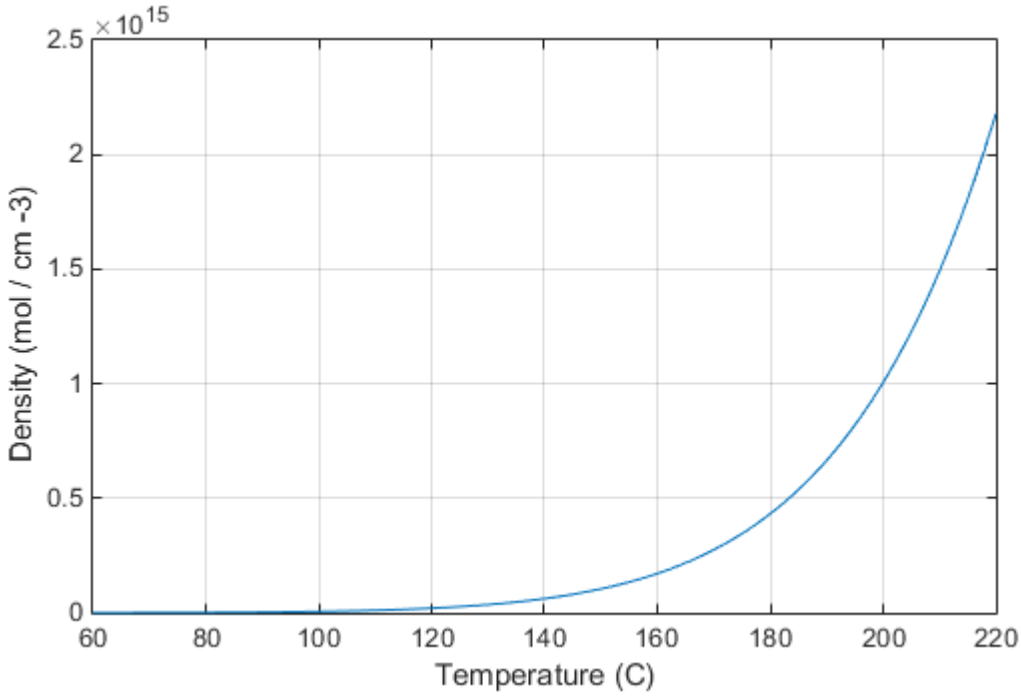

Figure 2.1. Rubidium vapour density as a function of temperature

Secondly, the separation between D1 and D2 transition energy lines of Rb is 14.7 nm allowing the use of common diode lasers with much narrower spectrum, typically 0.3~2 nm.

Rubidium has two stable isotopes ^{85}Rb and ^{87}Rb with natural abundancy of 72.2% and 27.8% respectively. It has the atomic number of 37 and the electron structure of $1s^2 2s^2 2p^6 3s^2 3p^6 3d^{10} 4s^2 4p^6 5s^1$ = [Kr] $5s^1$. The spin-orbit interaction quantized in the Bohr model lowers the 5s energy level below 4d and 4f energy levels, thus Rb is characterized by a single electron in the 5s orbital in the $5^2s_{1/2}$ state. This letter notation, known as spectroscopic notation, represents the angular momentum quantum numbers of states in atomic physics and has the form of $N^{2S+1}L_J$ where

N: the principal quantum number (often be omitted)

S: spin quantum number

2S+1: the number of spin states

L: orbital angular momentum denoted by letters as the following table:

L	**0**	**1**	**2**	**3**	**4**
letter value	s	p	d	f	g

Table 2.1. orbital angular momentum and corresponding letter values. The letters follow alphabetical order after g.

J: total electron angular momentum ($\vec{J} = \vec{S} + \vec{L}$).

^{85}Rb and ^{87}Rb energy levels schematic are shown in Figure 2.2. The first energy level is the Bohr energy level while spin-orbit, hyperfine and external magnetic field Zeeman splitting interactions are

consecutively added to the model. Bohr energy levels correspond to the orbital angular momentum and the coulomb interaction between the valence electron of Rb and the nucleus. These energy levels are separated by energies in the order of 1 eV. By further splitting, we have the fine structure substrates as a result of spin-orbit interaction in which the notation for the s state is $^2s_{1/2}$ and for the p state are $^2p_{1/2}$ and $^2p_{3/2}$. These notations can be achieved using the explanations from the previous paragraph. The electron spin quantum number S is ½, the orbital angular momentum L for s state is 0, and for p is 1, therefore the total electron angular momentum $\vec{J} = \vec{S} + \vec{L}$ is ½ + 0 = ½ for the s state, and is -½ + 1 = ½ and ½ + 1 = 3/2 for the *p* state. $5^2p_{1/2}$ and $5^2p_{3/2}$ are separated by energies in the order of 10^{-3} eV. The first excited state, $5^2p_{1/2}$, corresponds to D1 line of 794.7 nm, and the second one, $5^2p_{3/2}$, corresponds to D2 line of 780.0 nm.

Hyperfine states relate to the coupling between nuclear spin (I) and total electron angular momentum (J). It splits both $5^2s_{1/2}$ and $5^2p_{1/2}$ energy levels into two non-degenerate states labeled by F defined as total angular momentum $\vec{F} = \vec{J} + \vec{I}$. Since the nuclear spin for Rubidium-87 is I = 3/2, the values of F are ½ + 3/2 = 2 and -1/2 + 3/2 = 1 for the s state. A similar F values holds for the first *p* state, $5^2p_{1/2}$. These values for ^{85}Rb are ½ + 5/2 = 3 and -½ + 5/2 = 2. Hyperfine splitting is separated by energies in the order of 10^{-6} eV.

In the presence of an external weak magnetic field, each hyperfine state is further split into 2F + 1 Zeeman energy levels with quantum numbers of m_F = (-F, -F + 1, …, F + 1, F). Zeeman energy levels are proportional to the applied magnetic field, and are separated by energies in the RF range, ~0.5 MHz/Gauss for ^{85}Rb and ~0.7 MHz/Gauss for ^{87}Rb [31].

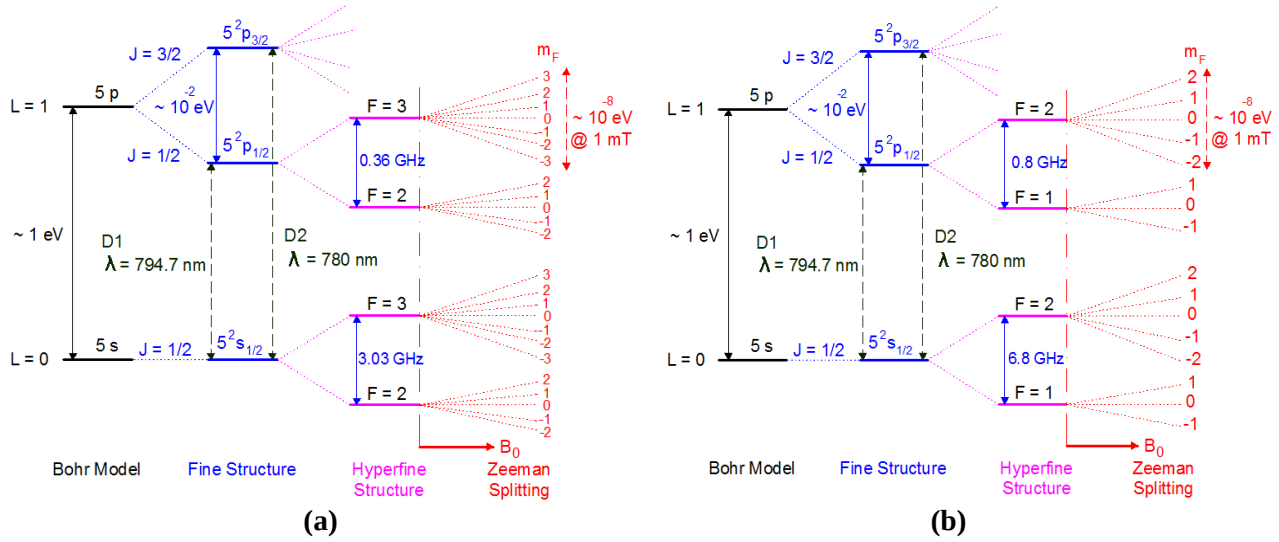

Figure 2.2. ^{85}Rb (a) and ^{87}Rb (b) energy levels (Not to scale). Spin-Orbit, Hyperfine and Zeeman splitting interactions are shown for each level.

All ground states ($5^2s_{1/2}$) are populated almost equally at room temperature. Electrons in ground states can transit to higher states ($5^2p_{1/2}$) if the incident beam wavelength corresponds to D1 transition line

(794.7 nm). The selection rules for the transition correspond to the incident photon polarisation with respect to the direction of the magnetic field. The right circularly polarised light, represented as $\sigma+$, occurs when the photons convey positive angular momentum with regard to the direction of the magnetic field. The light, represented as $\sigma-$, if photons convey negative angular momentum. No angular momentum is conveyed by the linearly polarised light known as π light. If a $\sigma+$ photon is absorbed, m_F increases by one. As can be seen in the Fig. 2.2.a, electrons in the all $5^2s_{1/2}$ sublevels of ^{87}Rb can absorb $\sigma+$ photons except the ones in the +2 sublevel since there is no +3 state in the $5^2p_{1/2}$ energy levels. When the incoming light is a π light, no change occurs in m_F. For the incident light of $\sigma-$, m_F decreases by 1. The lifetime of the electron in excited state is 10^{-8} – 10^{-9} s, then relaxes via photon emission to any m_F ground state sublevels based on the selection rule of $\Delta m_F = 0, \pm 1$. The emitted photon may be $\sigma+$, $\sigma-$ or π which can be absorbed as rotational or vibrational energy by buffer gases [46]. Continues transitions as a result of $\sigma+$ light absorption and afterwards relaxation will populate the highest ground state of F = +2 and m_F = +2 for ^{87}Rb and F = +3 and m_F = +3 for ^{85}Rb. For the $\sigma-$ light, the lowest ground state will be populated, i.e. F = +2 and m_F = -2 for ^{87}Rb and F = +3 and m_F = -3 for ^{85}Rb. Finally, when the highest or lowest ground state is saturated, the hyperpolarised rubidium necessary for hyperpolarising xenon is achieved.

2.2 Spin Exchange

Hyperpolarised xenon is achieved through spin-exchange collisions with polarised Rubidium. In the spin-exchange collision, the Rb electron magnetization is flipped by coupling with the nucleus spin of the xenon atom. This schematically can be depicted as:

$$Rb(\uparrow) + {}^{129}Xe(\downarrow) \rightarrow Rb(\downarrow) + {}^{129}Xe(\uparrow) \qquad (2.2)$$

The spin-exchange interaction can occur through two processes (Fig.2.3): Firstly, Rb-Xe binary collision involves sudden close contact of rubidium and xenon leading to spin-exchange between the two bodies. This process is more efficient at high pressures where collisions are more probable. Secondly, spin-exchange can occur during Rb-Xe long-lived van der Waals interaction. RbXe van der Waals molecule is formed through three body collisions:

$$Rb(\uparrow) + {}^{129}Xe(\downarrow) + Q \rightarrow RbXe(\downarrow\uparrow) + Q \qquad (2.3)$$

Where Q can be another xenon atom or a buffer gas usually nitrogen, helium or a mix of the two. The bond lifetime is approximately 10^{-7} - 10^{-11} s, then the RbXe molecule is broken through another Q collision. Q as a third body is required for energy conservation due to the bounding energy of ~ 20 meV for RbXe van der Waals molecule formation and destruction. van der Waals interactions are more dominant at low pressure systems where the Rb electron spin spends more time in the vicinity

of Xe atom which is a heavy noble gas with 54 electrons. The Hamiltonian of the spin-exchange is [47]:

$$\hat{H} = A\hat{\vec{I}}.\hat{\vec{S}} + \gamma\hat{\vec{N}}.\hat{\vec{S}} + \alpha\hat{\vec{K}}.\hat{\vec{S}} \tag{2.4}$$

where A, α and γ are the strength of angular momentum exchange reactions. The first term $A\hat{\vec{I}}.\hat{\vec{S}}$ is the magnetic dipole interaction between the Rb electron spin $\hat{\vec{S}}$ and the Rb nuclear spin $\hat{\vec{I}}$. The second term $\gamma\hat{\vec{N}}.\hat{\vec{S}}$ is the spin rotation interaction between the rubidium electron spin $\vec{S}$ and the rotational angular momentum of the RbXe molecule $\hat{\vec{N}}$. The last term $\alpha\hat{\vec{K}}.\hat{\vec{S}}$ gives the hyperfine coupling between the nuclear spin of the xenon $\hat{\vec{K}}$ with the electron spin of the rubidium $\hat{\vec{S}}$. This term of the Hamiltonian accounts for the Xe hyperpolarisation via spin-exchange collision with the polarised Rb. The degree of polarisation can be measured via NMR which will be discussed in more detail in the following section.

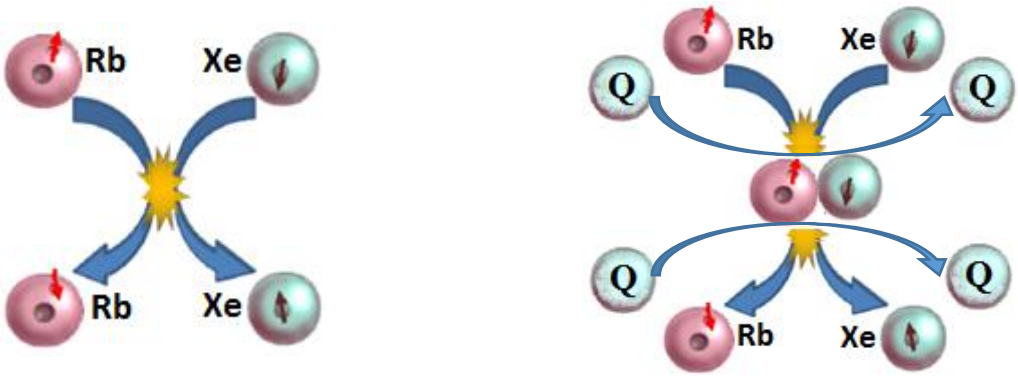

(a) **(b)**

Figure 2.3. Spin-exchange schematic for: a) Xe-Rb binary collision b) Xe-Rb van der Waals interaction involving Xe, Rb and a third body 'Q' such as buffer gases.

In addition to the critical role of noble gases in spin exchange process, there are other two major reasons for their presence in the optical pumping mixture: quenching of the excited state energy and D1 absorption line pressure broadening. Nitrogen has the major role of quenching the Rb excited states fluorescence. Uncontrolled emissions of σ+, σ- or π photons from the Rb excited $5^2p_{1/2}$ levels can be reabsorbed by polarised Rb atoms since they correspond to the D1 energy which leaded to a major Rb depolarisation effect. ^{4}He buffer gas is typically added to increase the total pressure inside the cell. The effect stands in broadening the D1 absorption line of the Rb vapour resulting in more absorbed light. The exact ratio of gases, however, is not critical to the spin exchange process. Typical ranges are from 1% to 5% Xe and 1% to 10% N_2 with the balance being He [48, 49].

2.3 Nuclear Magnetic Resonance

NMR is a physical phenomenon arising from nuclei with non-zero nuclear spin placed in a uniform magnetic field, $\vec{B}_0$. The $\vec{B}_0$ field acts upon the nuclei causing their spin to precess at the Larmor frequency along the axis of the field (typically the z-axis).

In typical NMR experiments, nuclei are polarised by a strong superconducting magnet (>=1.5T). The high magnetic field allows to form an unequal population of the energy eignstates through Boltzmann (thermal) polarisation. Hyperpolarisation, however, boosts the polarisation far beyond thermal equilibrium without the need of a powerful magnetic field for polarisation. It is conducted in a magnetic field of several mT with a resonance frequency range of kHz compared to 10 - 200 MHz for NMR experiments performing in high magnetic fields. As previously described, the polarised gas is achieved through SEOP. Low magnetic field NMR is required for detecting the degree of xenon polarisation and studying the dynamics of the polarised gas in the SEOP cell as a function of the gas operational temperature and pressure, and incoming photon flux. Using NMR as an analytical tool will allow us to find the best operational parameters of the polariser in order to maximize ^{129}Xe polarisation. The relevant NMR methods are briefly discussed in the following paragraphs. Further detail can be found in several textbooks [50, 51].

2.3.1 Mathematical Formalism of Spin Precession

Each nucleus has a unique configuration of protons and neutrons. Each of these nucleons, similar to what we described for electrons in Section 2.1, have an intrinsic spin angular momentum $\vec{S}$ as well as an orbital angular momentum $\vec{L}$ that is associated with their motion in the nucleus. The total nuclear angular momentum accounts for coupling between spin and orbital angular momentum, given by $\vec{I} = \vec{S} + \vec{L}$. All atomic nuclei with an odd number of protons or neutrons possess an intrinsic angular momentum $\hbar.\vec{I}$ which is proportional to the nuclear magnetic moment:

$$\vec{\mu} = \gamma.\hbar.\vec{I} \tag{2.5}$$

where $\hbar$ is the reduced Planck's constant or Dirac's constant (h/2π = 1.054571800 × 10^{-34} J.S), and γ is the gyromagnetic ratio specific for the kind of nucleus (for hydrogen protons γ_H = 42.577 $^{MHz}/_{T}$, and for ^{129}Xe nucleus γ_{Xe} = -11.777 $^{MHz}/_{T}$).

In an externally applied magnetic field $\vec{B}_0$, the nuclear magnetic moment interacts with the field. Suppose that $\vec{B}_0$ is in the z-direction ($\vec{B}_{0z}$) in the laboratory frame of reference, this leads to the interaction Hamiltonian equation:

$$\hat{\mathcal{H}} = \hat{\vec{\mu}}\,.\vec{B}_{0z} = -\gamma\hbar\vec{B}_{0z}.\hat{\vec{I}_z} \tag{2.6}$$

Where $\hat{\vec{I}}_z$ is the nuclear spin operator parallel to the field. The interaction Hamiltonian describes the interaction energy of the nucleus within the time-dependent Schrodinger equation. Suppose two wavefunctions $\varphi(t)$ and $\psi(t)$ describe the nuclear spin state of a single atom, thus both satisfy the same Schrodinger equation:

$$\hat{\mathcal{H}}\varphi(t) = -\frac{\hbar}{i}\frac{\partial\varphi(t)}{\partial t} \qquad \hat{\mathcal{H}}\psi(t) = -\frac{\hbar}{i}\frac{\partial\psi(t)}{\partial t} \tag{2.7}$$

The statistical average result of many measurements of the nuclear spin operator in the x direction ($\hat{I}_x$) defined by the expectation value is given by

$$\langle \hat{I}_x \rangle = \iiint \varphi^* \hat{I}_x \psi \, dV \tag{2.8}$$

The time derivation of the $\hat{I}_x$ operator can be written as

$$\frac{d\langle \hat{I}_x \rangle}{dt} = \iiint \frac{\partial\varphi^*}{\partial t}\hat{I}_x \psi \, dV + \iiint \varphi^* \hat{I}_x \frac{\partial\psi}{\partial t} \, dV \tag{2.9}$$

Combining equations (2.7), (2.8) and (2.9) will result in

$$\iiint \varphi^* \frac{d\hat{I}_x}{dt}\psi \, dV = \frac{i}{\hbar}\iiint \varphi^*(\hat{\mathcal{H}}\hat{I}_x - \hat{I}_x\hat{\mathcal{H}})\,\psi \, dV \tag{2.10}$$

With $[\hat{\mathcal{H}}, \hat{I}_x] = \hat{\mathcal{H}}\hat{I}_x - \hat{I}_x\hat{\mathcal{H}}$ the commutator of $\hat{\mathcal{H}}$ and $\hat{I}_x$, this equation results in the following Ehrenfest theorem for the average spin:

$$\frac{d\hat{I}_x}{dt} = \frac{i}{\hbar}\left[\hat{\mathcal{H}}, \hat{I}_x\right] \tag{2.11}$$

Substituting equation (2.6) into equation (2.11) yields

$$\frac{d\hat{I}_x}{dt} = -i\gamma\vec{B}_{0z}\left[\hat{I}_z, \hat{I}_x\right] \tag{2.12}$$

Using the cyclic commutation relations for the angular momentum operators, $[\hat{I}_z, \hat{I}_x] = i\hat{I}_y$, the x-component of the angular momentum operator is

$$\frac{d\hat{I}_x}{dt} = \gamma\vec{B}_{0z}\,\hat{I}_y \tag{2.13}$$

Similarly, for the y- and z-components of the angular momentum operators we obtain

$$\frac{d\hat{I}_y}{dt} = \gamma\vec{B}_{0z}\,\hat{I}_x \quad , \; \frac{d\hat{I}_z}{dt} = 0 \tag{2.14}$$

The three equations (2.13) and (2.14) can be summarized into the vector operation equation

$$\frac{d\hat{\vec{I}}}{dt} = \hat{\vec{I}} \times \gamma\vec{B}_{0z} \tag{2.15}$$

Since $\langle\hat{\vec{\mu}}\rangle = \gamma\hbar\,\langle\hat{\vec{I}}\rangle$, the equation for the expectation value of the spin angular moment becomes

$$\frac{d\langle\hat{\vec{\mu}}\rangle}{dt} = \langle\hat{\vec{\mu}}\rangle \times \gamma\vec{B}_{0z} \tag{2.16}$$

The resulting magnetization has components:

$$\mu_x = |\vec{\mu}|\sin\alpha\cos\omega_0 t \tag{2.17}$$

$$\mu_y = -|\vec{\mu}|\sin\alpha\sin\omega_0 t$$

$$\mu_z = |\vec{\mu}|\cos\alpha$$

where α is the angle $\vec{\mu}$ makes with the z-axis and ω_0 defines the speed of the precession movement known as the Larmor frequency:

$$\omega_0 = \gamma . B_0 \tag{2.18}$$

This set of equations describes the behavior of the magnetic dipole moments in the static magnetic field, and are known as Bloch equations.

2.3.2 Polarisation Detection Using NMR

The equation (2.15) was derived for the expectation value of the spin angular momentum of a single nucleus. For spin-1/2 particles, the total nuclear magnetic moment is measured through the projection of the mean spin vector onto the z-axis:

$$I_z = \frac{\hbar}{2} \left(P_{m=+1/2} - P_{m=-1/2}\right) \tag{2.19}$$

Where $P_{m=+1/2}$ and $P_{m=-1/2}$ are the probabilities to find the particle in the spin-up or spin-down states respectively. Having only two possible m states for a spin-1/2 particle, the total probability is equal to one:

$$P_{m=+1/2} + P_{m=-1/2} = 1 \tag{2.20}$$

Combining equations (2.19) and (2.20) gives

$$P_{m=+1/2} = \frac{1}{2} + \frac{1}{\hbar} I_z \tag{2.21}$$

$$P_{m=-1/2} = \frac{1}{2} - \frac{1}{\hbar} I_z$$

Thus, the distribution of particles in each spin state relates to the z-component of the nuclear spin. For thermal polarisation, the distribution corresponds to the Boltzmann statistics in equilibrium state. For hyperpolarised systems, however, it corresponds to the degree of polarisation. Polarisation along the magnetic field (z-axis) is referred to as longitudinal magnetization which is almost undetectable as it is several orders of magnitude lower than the field. In nuclear magnetic resonance imaging and spectroscopy, a different approach is taken. Instead of measuring the nuclear spin magnetization along the field, the magnetization perpendicular to the magnetic field is measured after the longitudinal magnetization is tilted over an angle of 90 degrees by use of a rotating magnetic field with the magnitude B_1 in the xy-plane. The total magnetic field is

$$\vec{B}(t) = B_0 \hat{k} + B_1 \cos(\omega t)\, \hat{\imath} - B_1 \sin(\omega t)\, \hat{\jmath} \tag{2.22}$$

Where $\hat{\imath}$, $\hat{\jmath}$ and $\hat{k}$ are constant unit vectors. Using equation (2.15) with this input magnetic field, and equation (2.21) with initial-state spin vector of $\vec{I}_z(t=0) = \frac{\hbar}{2}$, the probability of a transition from the spin-up to the spin-down state is found to be [52]:

$$P_{m=-1/2}(t) = \frac{1}{2} - \frac{1}{\hbar} I_z = \frac{(\gamma B_1)^2}{(\gamma B_1)^2 + (\omega - \omega_0)^2} sin^2(\omega' \frac{t}{2}) \tag{2.23}$$

Where

$$\omega' = \sqrt{(\omega - \omega_0)^2 + (\gamma B_1)^2} \tag{2.24}$$

The probability function (2.23) has a Lorentzian shape centred at the resonance frequency ω_0. Considering the B_1 field at $\omega = \omega_0$, this equation reduces to

$$P_{m=-1/2}(t) = sin^2\left(\frac{\gamma B_1 t}{2}\right) = \frac{1}{2}(1 - \cos(\gamma B_1 t)) \tag{2.25}$$

Assuming the magnetization begins in the up state, in order to flip the spin into the xy-plane (90° rotation), P(t) should be set to ½. Thus, the time required is

$$t_{\frac{\pi}{2}} = \frac{\pi}{2\gamma B_1} \tag{2.26}$$

This time for every other flip angle θ is

$$t_\theta = \frac{\theta}{\gamma . B_1} \tag{2.27}$$

Considering B_1, the net nuclear spin magnetization is now a vector rotating in the transverse (x-y) plane at the Larmor frequency. However, the transverse magnetization decays because the nuclear magnetic dipole moments dephase due to the local fluctuating magnetic field. This phenomenon is called relaxation which is characterized by spin-lattice or longitudinal (T_1) relaxation time and spin-spin or transverse (T_2) relaxation time. In hyperpolarised system, T_1 and T_2 relaxation behave in exactly the same way as in conventional MRI but that once the gas is in the patient, the longitudinal magnetization will relax towards the thermal equilibrium magnetization. Considering relaxation times, the Bloch equations are [53]:

$$\mu_x = |\vec{\mu}| \sin\alpha \, e^{-\frac{t}{T2}} (\cos\omega_0 t + \sin\omega_0 t) \tag{2.28}$$

$$\mu_y = |\vec{\mu}| \sin\alpha \, e^{-\frac{t}{T2}} (\cos\omega_0 t - \sin\omega_0 t)$$

$$\mu_z = |\vec{\mu}| \cos\alpha \, e^{-\frac{t}{T1}} + |\vec{\mu}|(1 - e^{-\frac{t}{T1}})$$

μ_z in Equation 2.28 shows that by time evolution, the magnetization will precess in the transverse plane while it eventually restores to equilibrium value $|\vec{\mu}|$. The $|\vec{\mu}|$ restoration time is characterized by T_1 and is caused by interactions between the nuclear spin magnetic moment and thermal motions of nearby molecules called 'lattice'.

The transverse magnetization is formed with the individual nuclei magnetization. The T_2 relaxation time is a measure of how long the transverse magnetization takes to decay. This type of relaxation is due to rapidly fluctuating magnetic field inhomogeneities caused by the moving electrons and nuclei.

3

Instrumentation and Experimental Setup

3.1 Polariser Concept

The polariser is an in house built batch mode polariser to produce small quantities of polarised ^{129}Xe gas. A schematic representation of the apparatus is presented in Figure 3.1. Before describing each compartment in detail, the experimental setup is outlined.

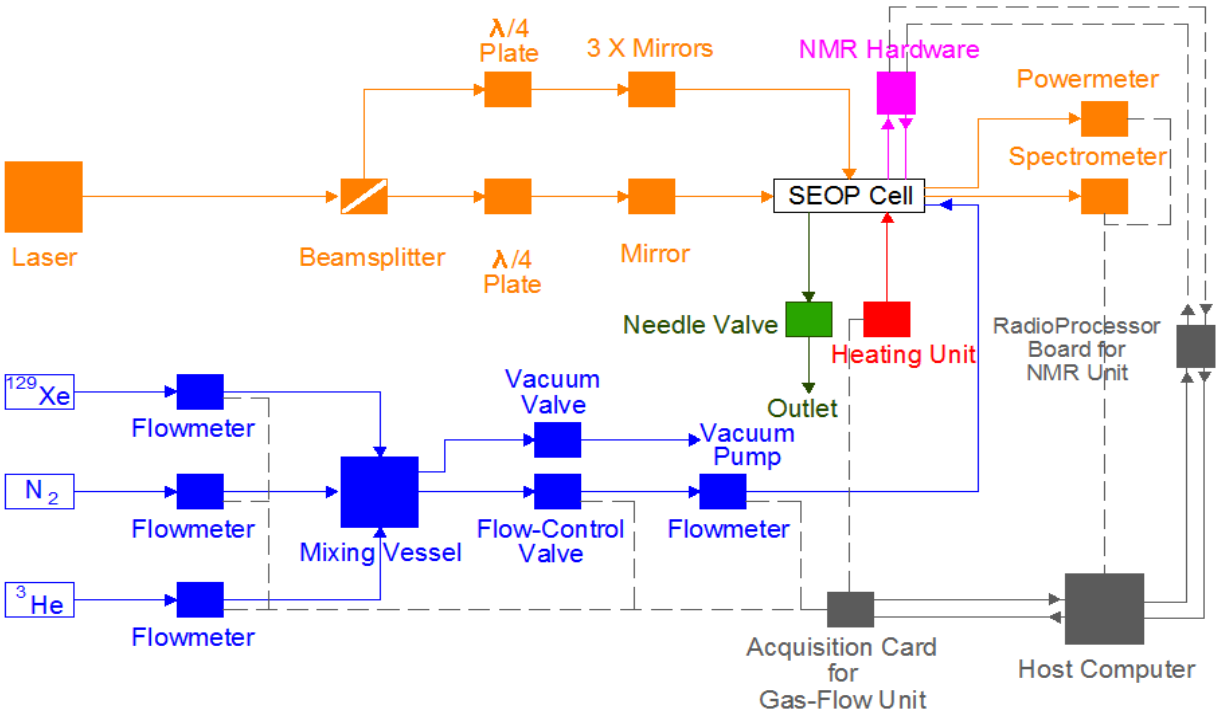

Figure 3.1. A simplified schematic drawing of the polariser. Different colors are used for different units: Gas-vapour flow system: blue; Optical path: orange; Heating unit: red; NMR hardware: pink; Gas extraction: dark green; Control Unit: gray.

The gas-vapour flow system: In this unit, three gases (^{129}Xe, N_2 and ^{4}He) are mixed in well-defined ratios. The gas mixture is saturated with Rb vapour into the SEOP cell through which a high power circularly polarised beam of laser light (794.7 nm) is directed.

The optical path: In order to generate a circularly polarised laser beam, a 30 Watt laser beam generated with a thermally stabilized diode array is guided through a beam splitter which linearly

polarises the light. Quarter-wave-plates convert the linearly polarised light in circularly polarised light. The laser light is directed through the SEOP cell. The residual laser light that exits the SEOP cell is stopped by a power meter which monitors the transmitted light. The spectrum of the light is recorded using an optical spectrometer.

The heating unit: In order to vaporise Rb, the SEOP cell is heated to 150 - 160°C by use of a heating wire and thermally isolated by use of glass wool. A thermocouple is used to monitor the temperature inside the SEOP cell.

NMR hardware: Once the nuclei of the ^{129}Xe atoms are polarised, the degree of nuclear magnetic polarisation is measured using an NMR polarimeter applying a Free Induction Decay (FID). A short radiofrequency (RF) pulse is applied by a set of transmit coils and the ^{129}Xe NMR signal is detected by a set of receive coil.

The gas extraction unit: When the mixture is evacuated from the cell, the gas is cooled down in a liquid nitrogen trap (-196 °C) to eliminate Rb vapour, and freeze the hyperpolarised xenon gas. Even in the solid state, the hyperpolarised gas exhibits a long T_1 relaxation time (4.1 hours/atm) while only a small permanent magnet is needed to maintain the polarisation. Frozen ^{129}Xe batches can be quickly thawed and dispensed into a gas sampling bag for delivery to the patient in the MRI scanner. As an example, Tedlar plastic bags with polypropylene valve fittings are non-permeable and easy to use in the scanner.

The gas-vapour flow unit is built on a vertical cabinet panel. The NMR, optics and SEOP components are installed on a separate horizontally orientated double cabinet shelves. The SEOP cell is suspended in a uniform magnetic field, B_0, in order to cause Zeeman splitting. The B_0 field is aligned along the z-axis.

3.2 B_0 Coils

The uniform magnetic field required for Rb optical pumping and NMR measurements is generated based on Helmholtz coils configuration. In principle, two identical coils with radius a_1, separated by a distance d_1 and carrying the same current I in the same direction will generate a uniform magnetic field on the centre. The field in the z-axis, B_{0a}, is simply measured by the sum of the two fields produced by the individual coils along this axis:

$$B_{0a}(z) = \frac{\mu_0 I}{2}\left[\frac{a_1^2}{((\frac{d_1}{2}-z)^2+a_1^2)^{3/2}} + \frac{a_1^2}{((\frac{d_1}{2}+z)^2+a_1^2)^{3/2}}\right] \quad (3.1)$$

Where μ_0 is the vacuum permeability, $4\pi \times 10^{-7}$ H/ m. In order to improve the field homogeneity in the SEOP cell region, we added another set of identical small coils to the Helmholtz configuration.

The field from these two additional coils needs to be added to the equation (3.1) to give the total field in the z-direction:

$$B_{0b}(z) = B_{0a}(z) + \frac{\mu_0 I}{2}\left[\frac{a_2^2}{((\frac{d_2}{2}-z)^2+a_2^2)^{3/2}} + \frac{a_2^2}{((\frac{d_2}{2}-z)^2+a_2^2)^{3/2}}\right] \quad (3.2)$$

Where a_2 is the radius and d_2 is the inter-coil distance of the added coils. The coils have previously been constructed in house, and were calibrated within this MRES project. They are built using 16 AWG copper wire on a PVC frame. The radius and the distance from the centre are shown in the Figure 3.2 for both two pairs of coils. The coils are driven by a EA-PS 8080-120 80V-120A DC power supply. In order to create magnetic field of 3.64 mT in the centre, the current was set to 6A. The current is monitored on a display on the power supply. The larmor frequency of xenon nuclei within this magnetic field corresponds to 42 kHz. NMR transmit and receive electronics are set to this frequency.

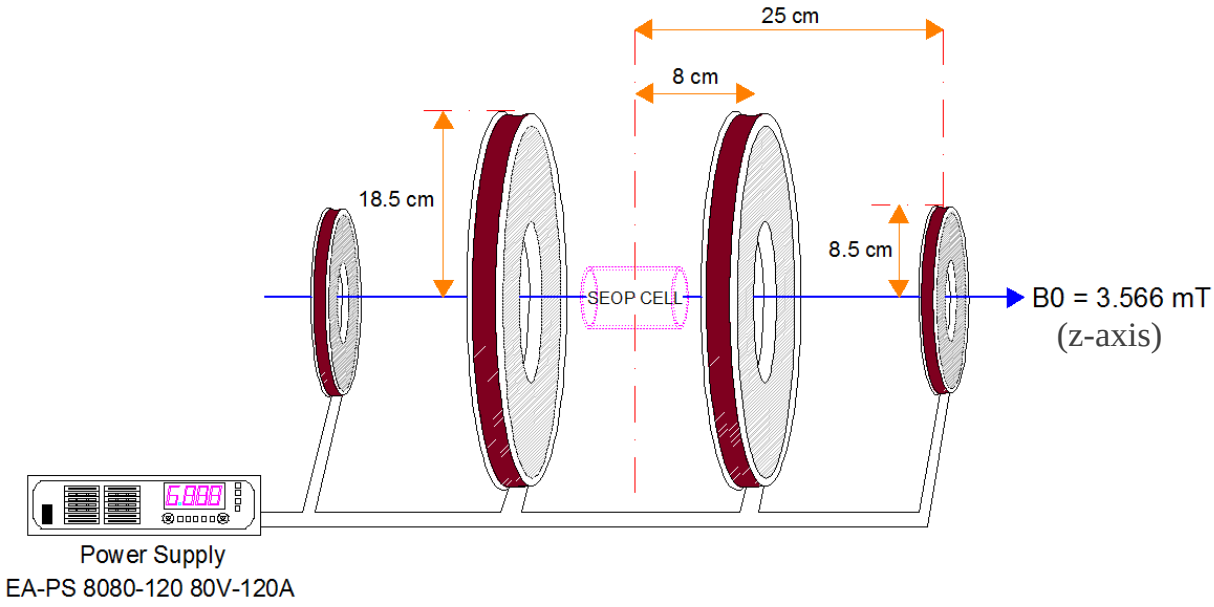

Figure 3.2. B_0 field generated using two pairs of Helmholtz coils. This configuration will generate a uniform magnetic field over 20 cm in the z direction.

The one-pair-coil and two-pair-coil configurations are simulated and the result is presented in Figure 3.3. The simulation shows that a homogeneity of ~1.2% for DSV (diameter of spherical volume) of 20 cm can be obtained using two-pair-coil configuration while this uniformity is less than 10 cm for one-pair-coil configuration. This is also in close agreement with experimental results. We measured inhomogeneity of 40 uT over 20cm region for the two-pair-coil configuration using a hall sensor (Honeywell, SS94A1F). The present SEOP cell is 10 cm long. A uniform field in a region as twice as this size allows us to increase the length of the SEOP cell to 20 cm for future upgrades of the polariser.

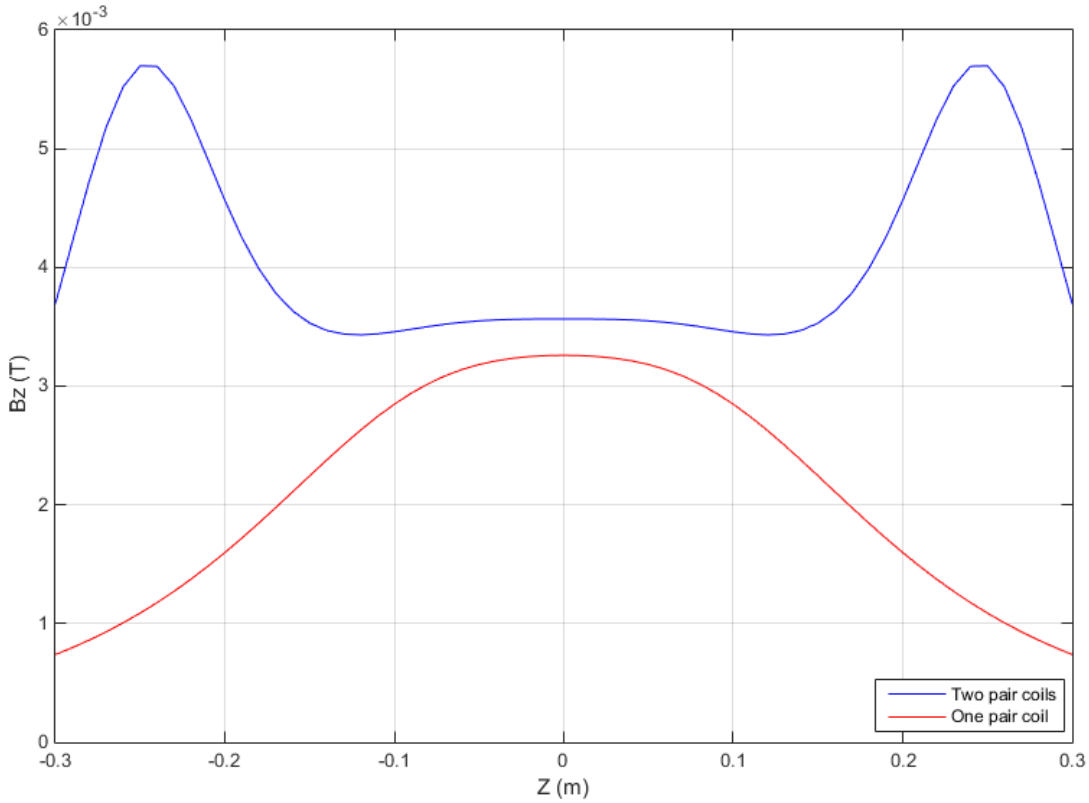

Figure 3.3. The magnetic field of the two-pair-coil vs one-pair-coil Helmholtz configuration along the z-axis. The field is uniform within 10 cm for the one-pair coil while uniformity increases over a 20 cm region for the two-pair coils.

3.3 The Gas-Vapour Flow System

In the gas-vapour flow unit, 5% xenon, 85% Helium and 10% Nitrogen by molar concentration are mixed in a mixing vessel, then transferred to the SEOP cell for further mixing with Rb vapour for optical pumping process. This previously built unit is further developed by adding an oxygen sensor and performing new design on the SEOP cell. A schematic of the flow system is shown in Figure 3.4, and explained in more detail as follow:

The Pyrex mixing vessel consists of a round bottomed flask with a five-vertical-tapper lid. The flask and the lid clamped on their flat flange and securely sealed with an O-ring. The vessel volume was measured to be 1.37 litres. From the five tappers of the vessel, two were connected to oxygen and pressure sensors. The oxygen sensor (Honeywell, GMS10 RVS) measures the O2 present into the vessel. An interface board (Honeywell, OXYMAC50) is considered for transducing the data from the oxygen sensor to the control system of the gas-vapour flow system. The pressure sensor and its transducer (Omega, PX309-030GV, 0-2.04 atm) measure the pressure in the vessel and transmit the data to a benchtop display (Omega, PCI41-030-S2) located on top of the gas unit. The display only shows the pressure within the range of 0.88 atm to 2.04 atm. Thus, an in house built transducer board with three pressure sensors are additionally provided on a sample line, branched from the vessel outlet. Pressure sensors are from Freescale Semiconductor: MPX4250A measures 1.18 to 3.45 atm, MPXV5100G measures 1 to 1.97 atm and MPXV6115 measures vacuum pressure from -0.14 to 1atm.

MPX4250A is not applicable for our present tubing system since the pressure would not exceed 1 atm.

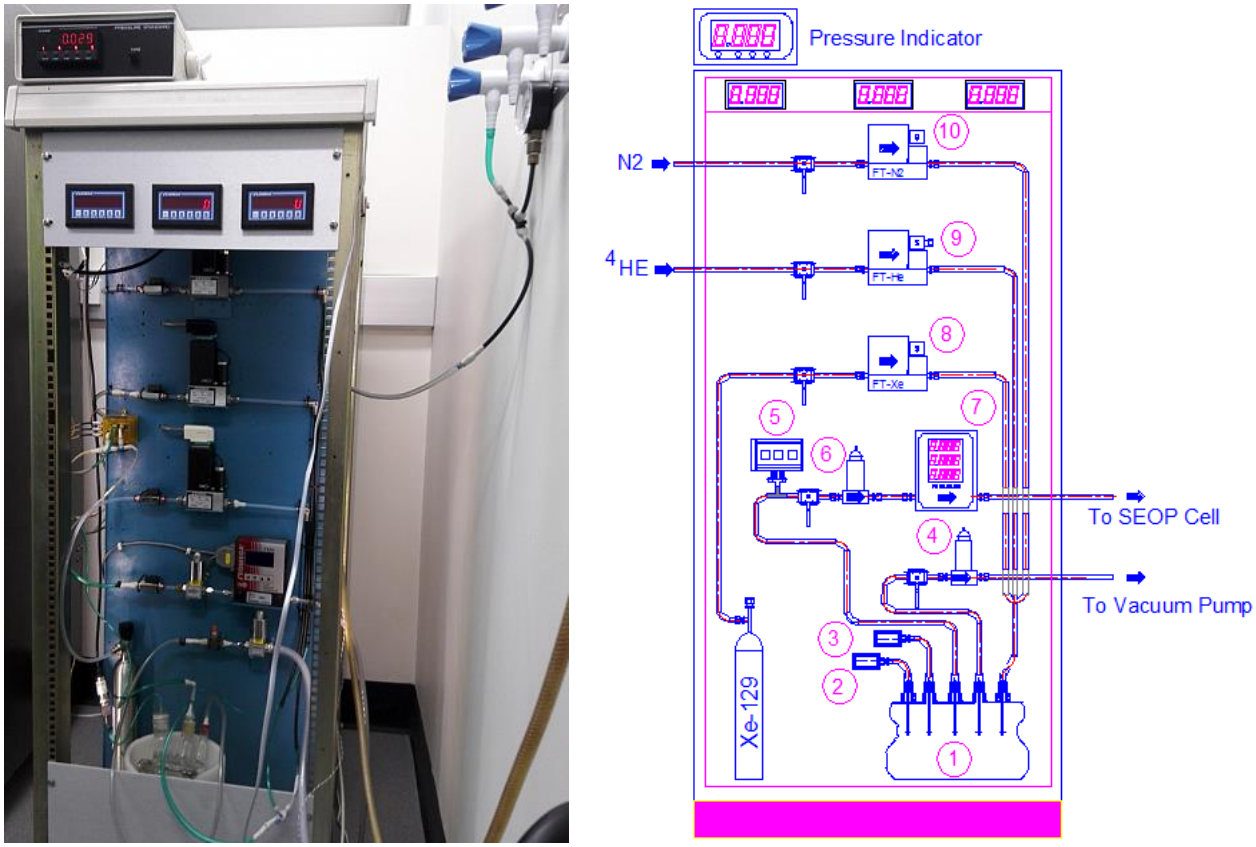

Figure 3.4. The gas flow unit and its schematic. 1) Mixing vessel; 2) Pressure sensor (0-2.04 atm); 3) Oxygen sensor; 4) Proportional solenoid valve for vacuum; 5) Three pressure sensors in the sample line; 6) Proportional solenoid valve for outlet; 7) Flowmeter in the outlet; 8&9&10) Flow controllers for Xenon, Helium and Nitrogen respectively.

The third tapper is considered for three gases, ^{129}Xe, N_2 and ^{4}He. Three gases from three paths are connected to an adapter ($3 \times {}^{1}/_{4}{}^{"}$) before entering the vessel. Flow rates are controlled for each gas individually by three mass flow controllers (OMEGA, FMA-7104E 150PSI/15PSI) with the flow range of 0 to 200 cm^3/min (at 1 atm and 0 °C), the maximum inlet pressure of 10.2 atm, and the maximum 1.02 atm pressure for the outlet. The pressure of the mixing vessel, thus, should not extend beyond 1.02 atm to avoid possible damage to the flow meters. The calibration of the flow controllers was done for each of the specific gases by manufacturer.

The vessel is vacuumed through its forth tapper via a Busch single stage rotary vane vacuum pump (R5 RA0063-0100F) with a minimal achievable pressure of 7×10^{-4} atm. A manual vacuum ball valve (Millsom Material Handling, KVZ-8) in addition to a proportional solenoid valve (Omega, FSV-15) are provided into the vacuum path since the proportional valve is not designed to work in high vacuum pressure.

The fifth tapper on the vessel serves as gas output. It delivers the gas mixture to the cylindrical sealed SEOP glass cell via a two-meter silicone tube. With cross section, the polariser glass cell is

placed (in the NMR cabinet shelves) one meter away from the gas-flow panel. Before delivery to the glass cell, the exhaust gas passes through a digital mass flowmeter (Omega, FMA6709, 0-5 L/min) via a proportional solenoid valve (Omega, FSV-15).

The cylindrical SEOP cell (diameter: 60 mm, length: 95 mm) has two side wings. One for inlet and one for outlet and thermocouple. The inlet connects the cell directly to the gas-flow panel outlet and vacuum pump via a twin vacuum-gas adapter. The vacuum route is isolated from the delivery route by a vacuum ball valve. The twin vacuum-gas adapter is isolated from the cell via a glass stopcock. This design allows us to remove the glass cell from the cabinet shelves with the closed stopcock as rubidium is inside. In order to vaporise Rb, the SEOP cell is heated to 150 - 160°C by use of a heating wire supplied by a DC power supply (Tenma, 72-10480). The wire is adhered to the cell wall by a tailpipe sealer that can withstand the high temperature of up to 1000°C. The cell outlet is only coupled with a screw cap in which a homebuilt J-type thermocouple is set to monitor the temperature inside. Once the gas is hyperpolarised, the outlet will be connected to the gas extraction unit. The thermocouple consists of two 5-meter wires (iron (JP) and constantan (JN)) twisted and spot weld at the junction at the end. The cell is thermally isolated by use of glass wool, and is positioned into a cylinder horizontally oriented on the centre of B_0, B_1 and pickup coils. The cylinder is made of Ultem 1000, polyetherimide resin (PEI), and fixed using a frame with the same material on a plate in the NMR cabinet shelf.

All flow and pressure controllers are computer regulated through an Extended USB interface card (Velleman, K8061). The card has 8 channels as analog inputs, and 8 channels as digital inputs. Three of the analog channels are associated with the three pressure sensors as previously mentioned. The forth channel is wired to the oxygen sensor. Three are occupied by the three mass flowmeters, and one is considered for the oxygen sensor. Two of the digital channels are connected to the two proportional solenoid valves. Three are wired to the three mass flowmeters which have internal solenoid valves. Three spares are left from the digital inputs.

Matlab is used to control the electronics, monitor and record the gas flow rates, pressures and temperatures.

3.4 Laser and Optics

The optical setup that has been followed in this study to polarise Rb vapour was already prepared. It can be described in four main stages:

Stage 1- *Laser:* Beginning with the laser, light is produced in a Helight Raylas Continuous-Wave (CW) Laser Diode Arrays' (LDA's) and exits through a 600 nm fibre. CW-LDA's are common in optical pumping experiments because of high power, compactness, and low cost. Our 30W LDA provides 794.4 to 795.4 nm wavelength light that is tunable with a +/- 2 nm range by specifying laser

current and the base cooling temperature. The laser current ranged 0-50A is controlled by a separate VueMetrix Vue-HCT Controller which combines a high current laser diode driver with an integrated temperature servo for air cooling. Relevant laser parameters were characterized and the results are presented in Section 4.8.

For safety reasons, the laser power is equipped with four interlocks. One interlock will also activate/ deactivate a flashing light to warn other researcher in the lab that the laser is on/ off (Fig 3.5, a.1). An emergency stop push button is considered on the front panel (Fig 3.5, a.2) and an on/off turn key is considered on the laser controller (Fig 3.5, b.4). In addition, a failsafe interlock is provided just under the laser enclosure door on top that will switch off the laser system when the panel is open (Fig 3.5, a.3). Only when all the interlocks are closed, the laser power can be switched on.

(a) **(b)**

Figure 3.5. A 30 W Helight Raylas laser (a) with its VueMetrix Vue-HCT Controller (b). The laser is provided with four interlocks: a bench top on/off switch (a.1), an emergency push button switch (a.2), a failsafe door interlock (a.3), and an interlock key switch on the controller (b.4).

Stage 2- *Optics:* The laser output fibre is attached to a fibre optic positioner (Melles Griot, 07 HFO 001) which provides precise alignment of fibre in two axes (XY). The laser beam is then directed to a symmetric-convex singlet lens collimator (Melles Griot, 01 LDX 103, f = 50 mm) producing a 5mm diameter beam. However, the linearly polarised laser light loses polarisation as it travels through the fibre. To fix this issue, beam passes through a polarising cube beamsplitter (Melles Griot, 03 PBS 057, 780 nm). However, the polarising cube has the inconvenience of splitting the incoming beam into two linearly polarised halves which need to be recombined. A pair of quarter wave plates (02 WRC 033, λ/4 Quartz Retardation Plate, 780 nm) converts these two outputs into circularly polarised light before recombining and reaching the SEOP cell using two different sets of mirrors (Fig. 3.6.) (>98% through combination of mirrors 6, 7 and 8, and <1% through mirror 9).

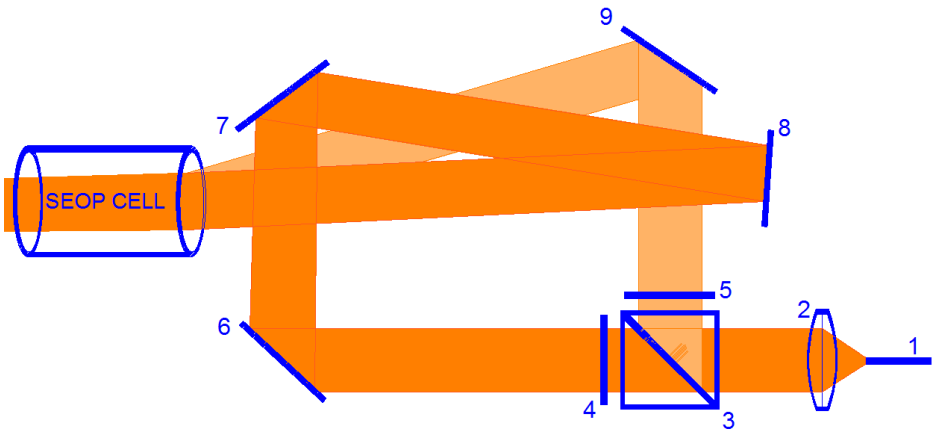

Figure 3.6. Optical setup for producing circularly polarised laser light: 1) fibre output; 2) collimating lens; 3) polarising beam splitter cube; 4&5) quarter-wave plates; 6&7&8) dielectric mirrors; 9) mirror at the focal point for beam combination (Not to scale, simulated on LightXLab)

Stage 3- *Laser light absorption:* the circularly polarised light enters the SEOP cell, and interacts with rubidium. Once Rb valence electron is polarised, the polarisation transfers to the xenon nuclei via collisions, as described in Section 2.1 and 2.2.

Stage 4- *Power and spectrum measurement:* The residual laser light that exits the SEOP cell is stopped by a power meter which monitors the transmitted light power. The power meter is a Gentec-EO model UP19K-50F-W5 with the following specification: 50W power, Fan-Cooled, grating "two"(diffraction grating centred on 750 nm with a spectral range of 0.19-10 µm), and a 17 mm effective aperture. Before being received by the power meter, the beam is converged using a plano-convex singlet lens (Melles Griot, 01 LPX 187, f = 100 mm). The spectrum of the light is also recorded by use of a high resolution optical spectrometer (HR2000, Ocean Optics). The spectrometer serves as the first indication of optical pumping and allows tuning to the correct wavelength 794.7 nm. When the cell is at room temperature, no light absorption is observed. Once the cell is heated up to a temperature so that a sufficient quantity of Rb vapour is present in the cell, while the B_0 coils are off, the laser light will be absorbed by the Rb, thus the laser's spectral peak will be attenuated. However, once the B_0 coils are turned on, optical pumping takes place, and the cell becomes more transparent to the incident laser light resulting in a renewed peak observed on the spectrometer. This phenomenon is shown in Fig. 3.7.

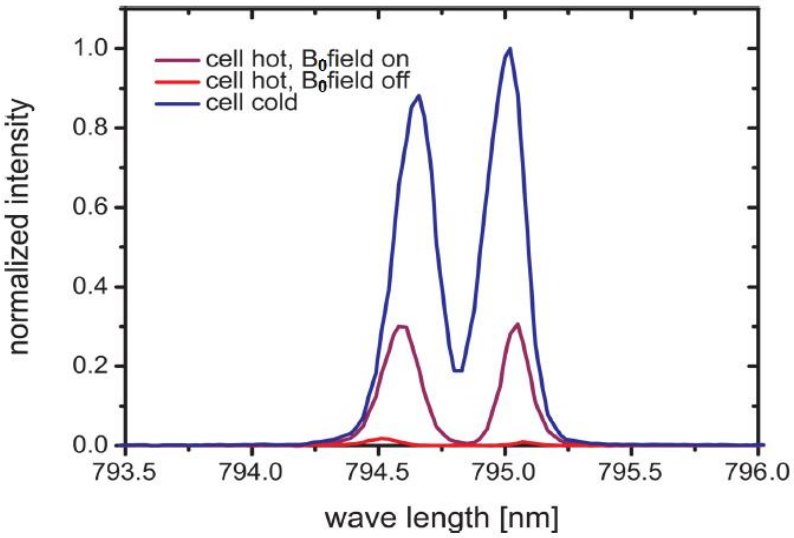

Figure 3.7. Laser spectrum for different pumping cell conditions. No absorption is observed for the cold cell (blue). However, the effect of optical pumping can be observed while turning the field B_0 on (violet) and off (red) [54].

A summary of the four stages are schematically shown in Figure 3.8. as follow.

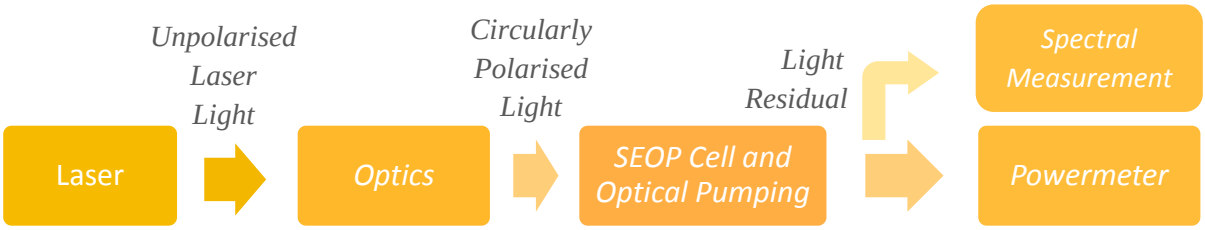

Figure 3.8. Block diagram of the optics configuration followed in this study.

3.5 NMR Hardware

A RF pulse is applied by use of a radioprocessor board. The pulse is amplified by an audio power amplifier and transmitted to a set of transmit-coils that are positioned at opposite sides of the SEOP cell. The impedance of the transmit coil is matched to 8 Ohms via a tuning-matching circuit. The ^{129}Xe NMR signal is received by another set of receive-coils. The receive coils are also tuned and matched to the input impedance of the receive circuit using two capacitors. The received signal requires amplification which is performed using two ultralow noise pre-amplifiers. The noise is swept from the signal using a low-noise band pass filter. After post-amplification the signal is recorded using the radioprocessor board for analysis. A trigger “TTL” level signal is generated by the board to control a transmit/receive switch. The TTL signal is defined as "low" when between 0 V and 0.8 V with respect to the ground terminal, and "high" when between 2 V and 5 V. The switch is to prevent leaking the transmit signal into the receive channel.

The schematic of the polarimeter hardware has been shown in Figure 3.9 and a detailed description is given in four sections as follow:

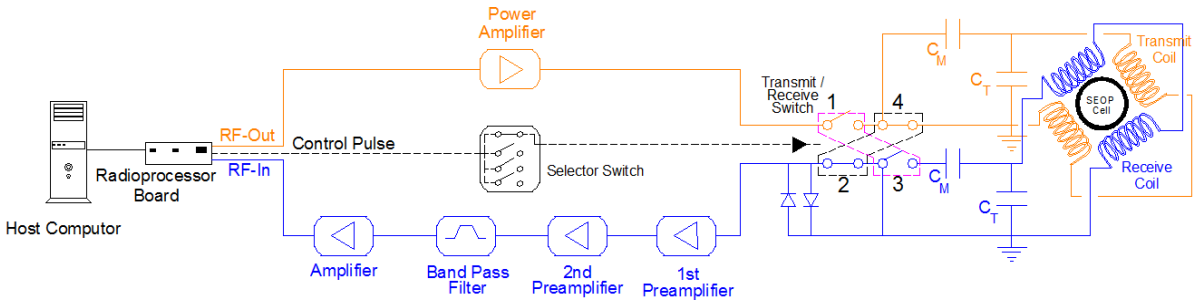

Figure 3.9. Schematic diagram of the NMR hardware, the transmit path is shown in Orange color while the receive path is presented in blue color. The control components are shown in black (Transmit/ Receive switch, two tuning-matching circuits and the second pre-amplifier have undergone new design within this MRES project. The rest of the equipment were already prepared).

3.5.1 RF Pulse Console

RF pulse is produced using a radioprocessor board (SpinCore Technologies Inc.,) (Fig 3.10.a). The board has a single 50Ω output channel to produce sinc or square pulses within a wide range of frequencies from 0 to 100 MHz. The received signal is recorded through the only 50Ω input channel on the board. The amplitude of the received signal should not extend 1.13V, otherwise the board can be damaged. A TTL control signal, generated by the acquisition card, is also used to activate a transmit/receive switch (Tx/Rx switch) to disconnect the transmit coil during signal reception and the receive coil during excitation.

The board is housed in an aluminum chassis with a USB power supply (Fig 3.10.b). The power supply converts a 12 VDC input supply voltage into three regulated voltages, +5V/2A, +6V/1A, and -6V/0.2A, as required by the SpinCore RadioProcessor board. A homebuilt 18VDC power supply and an adapter are used to generate 12VDC (Fig 3.10.c).

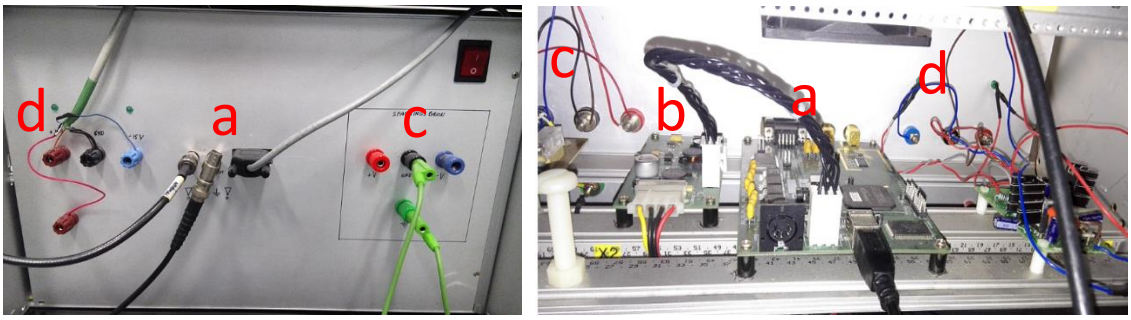

Figure 3.10. The front and back view from the RF pulse console with two homebuilt power supplies, a) Radioprocessor board, b) 12 VDC USB power supply of the board, c) ±18 VDC power supply and the converter 12 VDC d) ±15VDC-GND power supply required for receive path components.

3.5.2 Transmit Path

The produced RF pulse is amplified by a commercial audio power amplifier (Boyin, BN-250) with 20 kΩ input impedance. The power amplifier has the frequency response of 10 Hz-50 kHz (-1.5 dB) which covers our centre frequency 42 kHz with 0.5 kHz bandwidth. We set the amplifier on the bridge mode. In bridge mode, two amplifier's output channels are wired in series to give us the 8 Ω output

impedance and more output power 700W with the maximum gain of 21 dB. The amplified pulse will be transmitted to a set of transmit-coils via a Tx/Rx switch. The impedance of the transmit coil is matched to 8 Ω via a tuning-matching circuit. This circuit consists of two tuning (C_T = 3.25 nF) and matching (C_M = 16.9 nF) capacitors. The method of calculation of the two capacitors will be discussed in Section 4.4.

3.5.3 Transmit and Receive Coils

Two separate coils are applied for transmit and receive paths. This allows us to match their impedances more appropriately with their relevant electronics at resonance. The coils are linearly polarised, and positioned perpendicular to each other around a cylindrical tube (diameter d = 8 cm and height h = 12 cm) in order to avoid mutual coupling. Coils are surface type wound on a rectangular form made of Borax™. Transmit coils are connected in series by an ordinary 50 Ω coaxial cable similar to received coils. The receive coils are tuned and matched to the input impedance of the receive circuit using two capacitors (C_T = 47 pF and C_M = 415 pF). The transmit coils are also tuned and matched to 9.25 Ω of the input impedance. The configuration is shown in Figure 3.11, and the other features are listed in table 3.1.

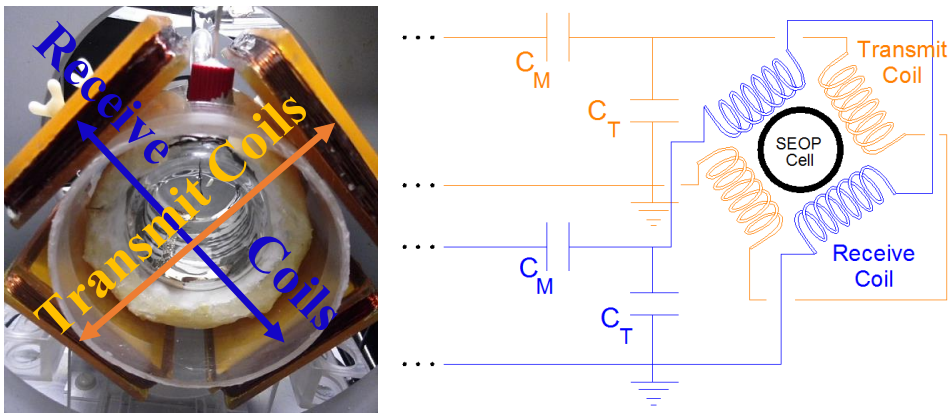

Figure 3.11. Transmit and receive coils and the schematic of their configuration around the SEOP cell.

	Transmit Coil	**Receive Coil**
Inductance	L1: 0.358 mH L2: 0.355 mH L(total) = 0.713 mH	L1: 11.93 mH L2: 11.9 mH L(total) = 23.83 mH
Total resistance: R = R1 + R2	R1: 0.493 Ω R2: 0.487 Ω R(total): 0.98 Ω	R1: 21.2 Ω R2: 21.4 Ω R(total): 42.6 Ω
Frame Size on each side	12.5 cm × 8.5 cm × 1 cm	12.5 cm × 8.5 cm × 1 cm
Turns	70 (35 windings on each side)	260 (130 windings on each side)
Wire type	20 AWG copper solid wire	30 AWG copper solid wire
Resistance of the wire	0.0333 Ω/m	0.338 Ω/m
Measured AC impedance @ resonance of 42 kHz	~ 12 Ω	3.3 kΩ

Table. 3.1. Transmit and Receive coils characteristics.

3.5.4 Receive Path

The received FID signal is pre-amplified within two stages. Preamplifiers are built in house using ultralow-noise (1 nV/√Hz) and ultralow-distortion (-120 dB) op-amp AD797A. For lowest noise, the op-amp is performed in the non-inverting mode, and the equivalent resistance of the feedback network is kept as low as possible (R_F + R_{IN}) resulting in a low gain of 20 dB. The configuration is shown in Figure 3.12. Two 20 dB low-gain preamplifiers are applied in series to have a desired gain. A circuit with OP177 is also applied as an isolating interface between two stages as the input impedance of the AD797A is as low as 7.5 kΩ.

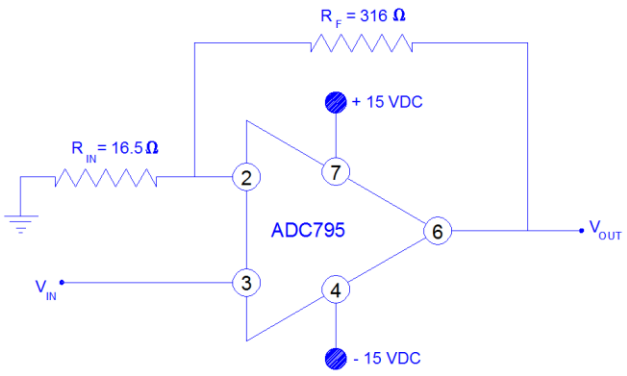

Figure 3.12. Preamplifiers' circuitry with gain Av = 20, the feedback resistor is kept as low as possible to keep the noise at the lowest level

Pre-amplification is followed by a band-pass filtering with a centred frequency at 42 kHz. This filter is an 8th order homebuilt low-noise bandpass filter with a single 5V power supply. The Q factor for the filter is ≈ 6. The circuitry and the frequency response are shown in Figure 3.13.

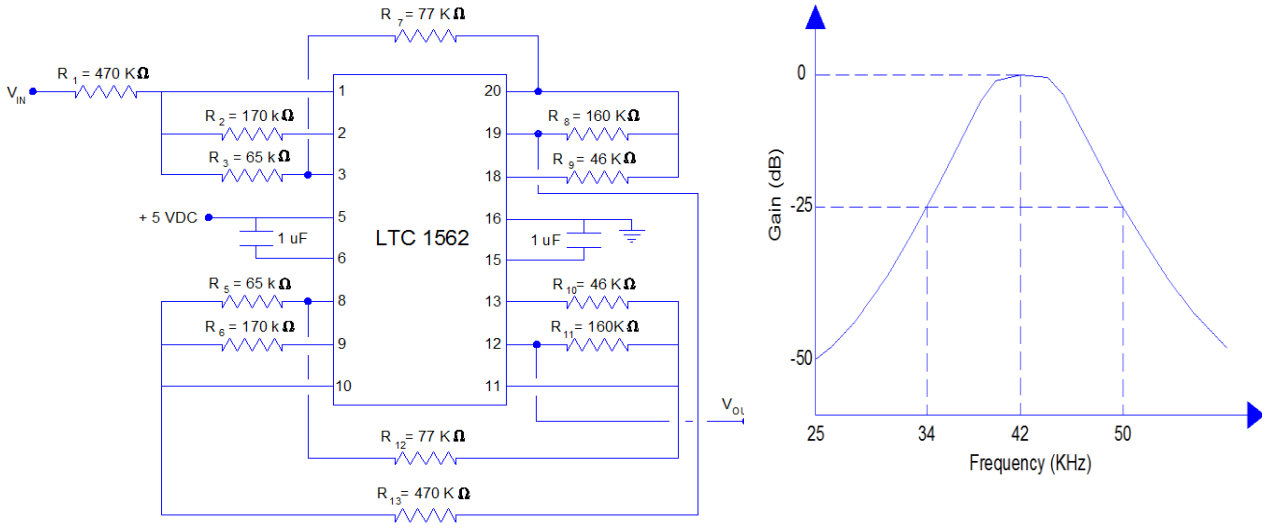

(a) (b)

Figure 3.13. Bandpass filter circuitry and frequency response, the circuit was designed in a way that the frequency is centred at 42 kHz.

The received signal is finally amplified with a post-amplifier MITEQ AU-1332 with the gain of Av = 60 dB, and 50 Ω input and output impedance before being processed by the Radioprocessor board.

3.5.5 Transmit/Receive switch

The receive NMR signal is several orders of magnitude lower than the transmit RF pulse. Therefore, it is essential that no residues of the transmit signal leak into the receiver channel of the acquisition card. This is achieved by designing a new efficient Tx/ Rx switching circuit for the polariser. The switch is controlled by the TTL control signal generated by the SpinCore radioprocessor board. The circuit is built in house using MAX4580 and MAX4690 analog switches feature low on-resistance of 1.25 Ω. The MAX4580 has two normally closed (NC) switches, and the MAX4690 has two normally open (NO) switches. The switching circuit is placed into a RF-shielded Faraday cage chassis. A schematic of the circuit is shown in Figure 3.14.

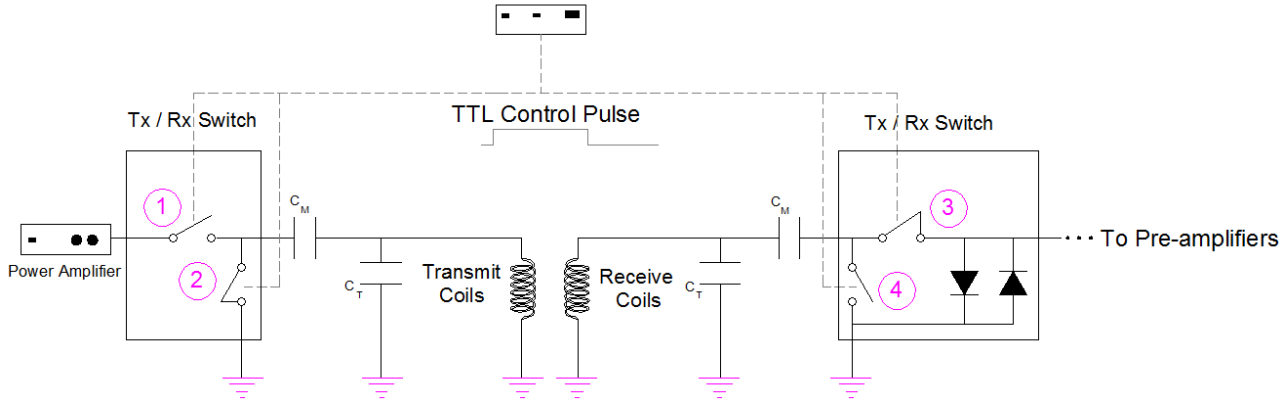

Figure 3.14. Transmit/ Receive switch configuration. Switches 1&4 and switches 2&3 are related to MAX4580 and MAX4690 respectively. 1.25 Ω on-resistance of the switches is not shown.

During transmission, TTL control pulse sets the switch-1 to "on" (closed) allowing the transmit RF pulse coming from the power amplifier to pass through the transmit coil. The receive path is disconnected since switch-3 and switch-4 are "off" (open), and "on" respectively.

During receive, the switch-3 is set to "on" allowing NMR signal to flow through the receive path. The "off"-switch-1 and "on"-switch-2 disconnect the power amplifier from the transmit coils. Crossed diodes are additionally shunted at the ground input of the pre-amplifiers to clip overvoltages to the ground.

All electronic circuits are separately placed within RF-shielded Faraday cage chassis to prevent electronics from picking up spurious signals from the other components.

4

Results and Discussions

This chapter will provide calibrations for different parts of the polariser and discuss measurement results, calculations and operational technique needed to operate the polariser. These achievements were acquired within this MRES project.

4.1 B_0 Calibration

Two pairs of two identical Helmholtz coils built in house are considered to generate the homogeneous magnetic field in the polarising glass cell as discussed in Section 3.2. The coils are driven using EA-PS 8080-120 80V-120A DC power supply, and the current through the coils is monitored on its display. The magnetic field in the NMR region was measured using a hall sensor (Honeywell, SS94A1F) with a sensitivity of 25 mV/Gauss. The Hall sensor was positioned in the region perpendicular to the z-axis. The current through the coils was increased in 1A increments. We recorded an increase in magnetic field for ~0.5 mT/A on average. The result is presented in Figure 4.1. The low magnetic field of 3.56 mT was chosen arbitrarily since the impact of a low field on RbXe van der Waals molecule interaction is small. The corresponding current to this magnetic field is 6A. The NMR Larmor frequency at this field is 42 kHz for ^{129}Xe nuclei.

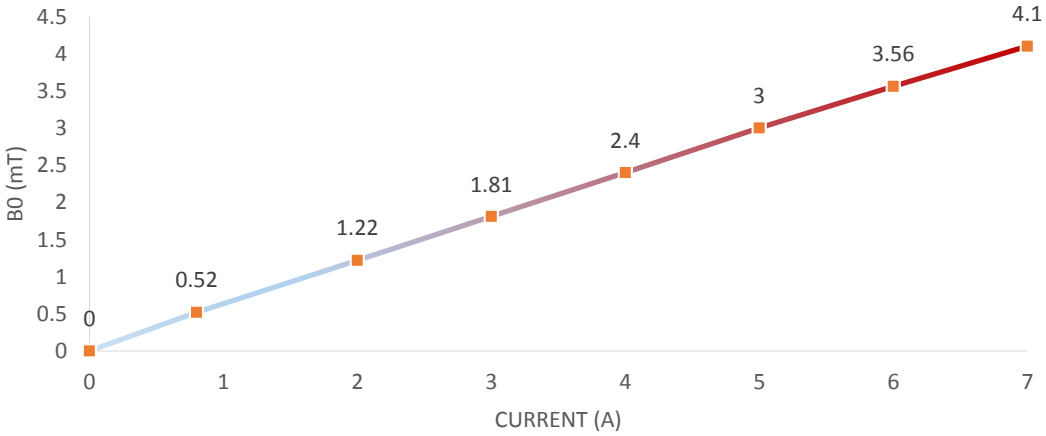

Figure 4.1. B_0 calibration. The solid line shows the magnetic field corresponding to the current through the B_0 coils within the NMR region.

For measuring field inhomogeneity, the sensor was located in different positions within the polarising glass cell, and changes in its output voltage were monitored. A 1.2% uniformity over a 20 cm DSV was observed which corresponds to a bandwidth of ~0.5 kHz.

4.2 B_1 Calculation

The radiofrequency pulse through the transmit path generates B_1 field within the transmit coils causing magnetization flip into the transverse (xy) plane (Section 2.3). The duration and amplitude of the RF pulse will identify the flip angle. The relationship between these three factors was shown in equation 2.27 ($\theta = \gamma_{Xe}.B_1.t_\theta$). Assuming a $\frac{\pi}{2}$ RF pulse within a time span $t_{\frac{\pi}{2}}$ of 1 ms, B_1 is equal to -21.227 µT. The current through the transmit coils corresponding to this field can be calculated from Biot-Savart's law. According to Biot-Savart's law, the magnetic field at any point of a wire due to the current can be obtained by adding up the field contributions, dB, from small segments of the wire dL. The transmit coil in our case has a rectangular shape ($\frac{L_1}{2} = 6.25\ cm$ and $\frac{W_1}{2} = 4.25\ cm$) with a $a \approx 5.25\ cm$ distance from the centre as shown in Figure 4.2.

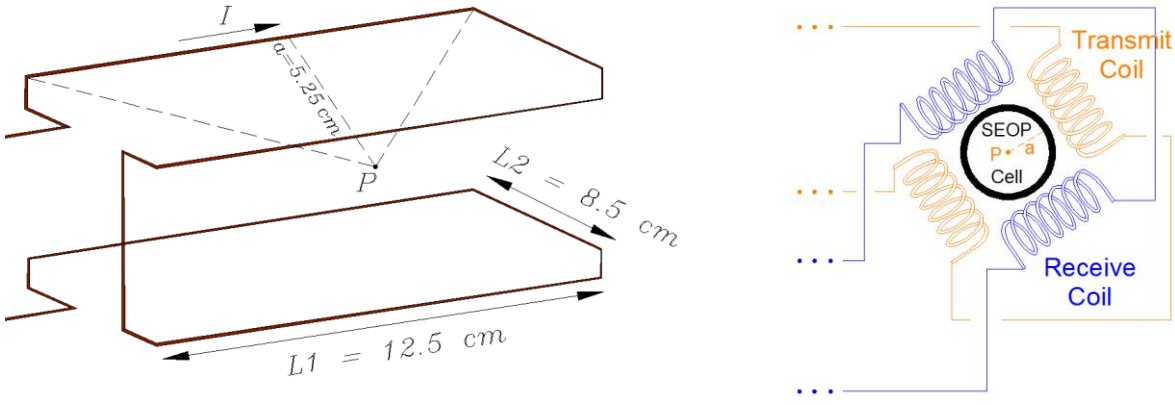

(a) **(b)**

Figure 4.2. B_1 coil configuration and shape (a) and its position in regard with the SEOP cell and received coils (b) (Not to scale).

The magnetic field for each of the straight wires of a single rectangular coil carrying current I, at the centre of the coils is

$$B = \frac{\mu_0.I}{2.\pi.a}\frac{L'}{\sqrt{L'+a^2}} \tag{4.1}$$

Where L' is the half-length of the wire.

The total magnitude of the field for the rectangular shape coil with N windings is the sum of four contributions as follows

$$B_1 \cong \frac{N.\mu_0.I}{\pi.a}\left[\frac{L_1'}{\sqrt{L_1'+a^2}} + \frac{L_2'}{\sqrt{L_2'+a^2}}\right] \tag{4.2}$$

Considering a half factor arises from the linearly polarised coil, the current is 26.55 mA. Having the impedance magnitude of the coil, Z = 188.2 Ω (L = 0.713 mH, R = 0.98 Ω), the required voltage across the transmit coil to excite the xenon nuclei for 90 degrees is ~5 V. These calculations were done for different flip angles and pulse time. The result is presented in Table 4.1.

Flip Angle (θ)	Pulse Time (t_θ) ms	B_1 Field μT	Current through the Coils mA	Voltage Across the Coils V
$\pi/2$	1	-21.227	26.55	5
$\pi/6$	0.5	-14.15	17.7	3.33
$\pi/4$	2	-5.3	6.63	1.25
$\pi/2$	2	-10.61	13.25	2.5

Table 4.1. Flip angle calibration based on different pulse time.

To generate the voltage corresponding to the right flip angle across the coil, the transmit signal must accordingly be calibrated. This will be discussed in detail in the Section 4.4.

4.3 NMR Pulse Sequence

The NMR pulse sequence is performed by the SpinCore RadioProcessor board as follows: A blanking TTL pulse is applied to allow the power amplifier to warm-up (Blanking Delay), and to close the normally-open transmit switch to let the signal pass through (TTL Blanking). A single "sinc" RF pulse is applied (Pulse Time). The induced high voltage on the transmit coils is allowed to ring down (Transient Time), and the FID signal is captured (within the length of Acquisition Time). The xenon nuclei are then allowed to relax for a specified amount of time (Repetition Delay). This scan sequence can then be repeated for an arbitrary number of times as desired to improve the SNR. The timing diagram of this scan is shown in Figure 4.3.

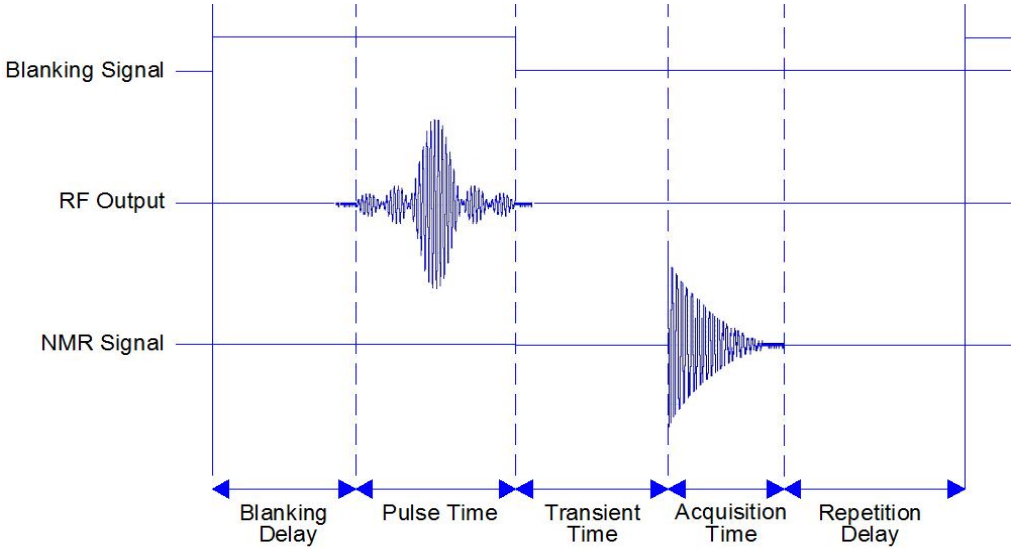

Figure 4.3. The timing diagram of a single-pulse sequence (Not to scale).

The source code of this sequence is in C-language, "singlepulse_nmr.c" which is proposed by the board manufacturer (SpinCore Technologies Inc.). A Matlab program is further developed within this project to control the whole transmit-receive process in which this C program is also called.

The Matlab program performs as follows: The input parameters of the program are first set by the operator. These parameters are listed in Table 4.2. After running the program, the received data is saved into an ASCII text file. The recorded data has real and imaginary components since the board has two internal channels for real (cosine) and imaginary (sine) component of the FID signal. The phase difference between these two channels is set within the C-program. This value is set to 90 degrees by default. Thus, the incoming real and imaginary signals are in the same phase. In this case, only one (the real) component is enough for analysis which will result in a symmetrical spectrum of the data (positive and negative frequencies). The negative frequencies can simply be removed from the Matlab program. If the phase is set to 0, for example, the magnitude of the complex data must be applied which is the square root of the sum of the squares of real and imaginary components. Thus, no phase correction is required. The default value for the phase difference is not changed in our program. The incoming real data is plotted in the time and frequency domains. A software low-pass filter is developed to suppress high frequency noise from the receive signal. Impulse response of the filter and the filtered signal are also plotted.

No.	Parameter	Description
1	BOARD_NUMBER	Radioprocessor board number if multiple boards are installed. We only have one, thus the value is set to 0.
2	ADC_FREQUENCY	Clock frequency of the board that is 75 MHz for our card.
3	ENABLE_TX	1 enables the transmitter and 0 disables the transmitter.
4	ENABLE_RX	1 enables the receiver and 0 disables the receiver.
5	REPETITION_DELAY	Delay between scans must be greater than 0 (See Figure 4.4).
6	NUMBER_OF_SCANS	Number of scans.
7	NUMBER_OF_POINTS	Number of complex (real and imaginary) points to be captured.
8	SPECTROMETER_ FREQUENCY	Spectrometer frequency which is 42 kHz in our case
9	SPECTRAL_WIDTH	Desired base band spectral width of the FID signal.
10	PULSE_TIME	Duration of the excitation pulse in μs (See Figure 4.4).
11	TRANS_TIME	The waiting time allowing the induced voltage on the transmit coils to ring down (See Figure 4.4).
12	TX_PHASE	Phase of the transmit signal in degrees.
13	AMPLITUDE	Transmit signal amplitude which is set between 0.0 and 1.0.
14	SHAPED_PULSE	1 is for a 'sinc' shaped transmit pulse, and 0 is for a square pulse.
15	BYPASS_FIR	1 bypasses the board internal filter, and 0 enables it.
16	FNAME	The file name to save the acquired data. The data is saved in a ASCII text format which will be imported and plotted into the Matlab Program.
17	VERBOSE	1 enables the output and 0 gives nothing.
18	BLANKING_EN	1 enables the TTL blanking signal transmission, and 0 disables it.
19	BLANKING_BIT	Specifies which TTL “Flag Bit” is applied for the TTL control signal. The board provides 9 digital output as TTL signal through a standard DB-9 connector. Each pinout refers to a “Flag Bit” number. Pinout 2 is connected in our board.
20	BLANKING_DELAY	Delay needed to warm-up the SpinCore RF power amplifier prior to the RF pulse (See Figure 4.4)

Table 4.2. Matlab program input parameters for controlling the radioprocessor board.

4.4 Transmit Path

Transmit path was discussed in Sections 3.5.2 and 3.5.3. The schematic diagram of the electronics is shown in Figure 4.4.

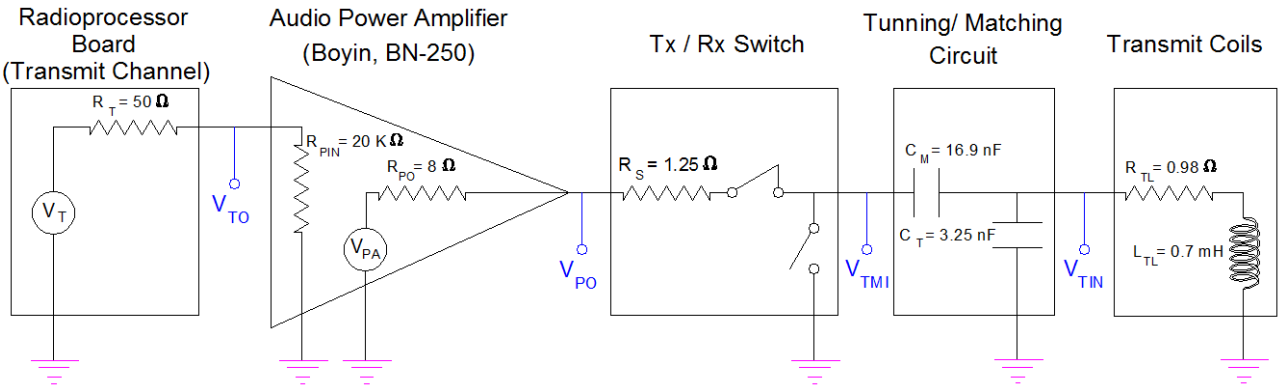

Figure 4.4. Electronic equipment of the transmit path with their input-output impedances. The impedance of the transmit coils is matched with the output impedance of power amplifier (R_{PO}) and on-resistance of the transmit-receive switch (R_S) via two capacitors C_M and C_T.

Calculation and measurement results are discussed in two sections: impedance matching and transmit signal calibration as follows:

***Impedance matching*:** The audio power amplifier has a 4 Ω impedance for each of its two output channels. It was set in bridge mode in which two channels were connected in series to give an overall 8 Ω impedance on output. The transmit-receive switch has also a 1.25 Ω on-resistance. Thus, the transmit coil should be tuned and matched with 9.25 Ω. Tuning-matching circuit consists of two tuning and matching capacitors (C_T and C_M) as is shown in Figure 4.5. The theoretical method of calculating these capacitors is discussed as follow.

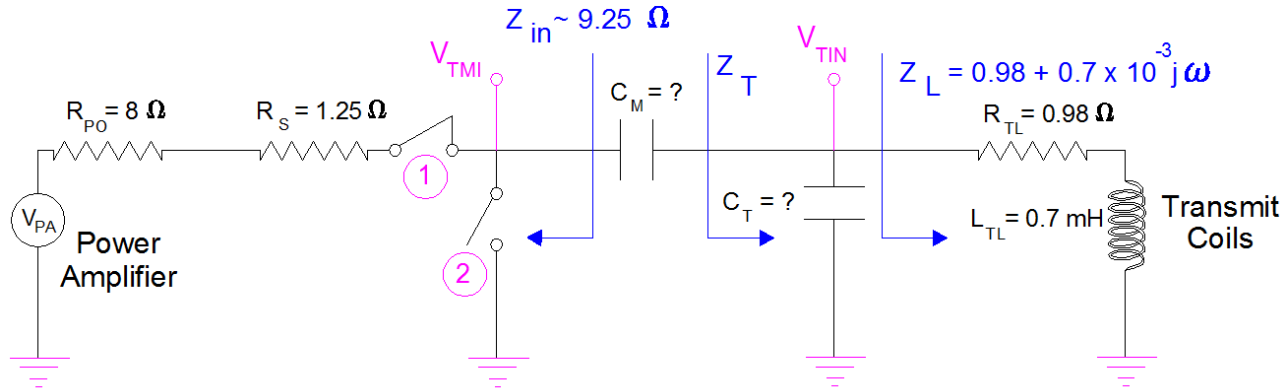

Figure 4.5. Impedance matching of power amplifier with Tx/Rx switch (shown in the "on" position) and transmit coils.

The tuning-matching procedure occurs in two steps; First, the resonant frequency of the transmit coils is adjusted by tuning capacitor C_T so that the real part of the impedance Z_T is equal to Z_{in} = 9.25 Ω at the spectrometer frequency of 42 kHz:

$$Z_T(Real) = \frac{R_{TL}}{(1-L.C_T.\omega^2)^2+(R_{TL}.C_T.\omega)^2} = Z_{in} \quad (4.3)$$

After some calculus, the tuning capacitance is found to satisfy

$$C_T = \frac{Q-A}{B.\omega} \quad (4.4)$$

Where

$$Q = \frac{L.\omega}{R} \quad (4.5)$$

$$A = \sqrt{\frac{B}{Z_{in}} - 1} \quad (4.6)$$

$$B = R.(1+Q^2) \quad (4.7)$$

From the equation 4.4, C_T was calculated to be 13.8 nF. Similarly, it can be shown that under matching conditions the imaginary component of the impedance becomes

$$Z_T(Imaginary) = Z_{in}.A \quad (4.8)$$

The impedance is inductive and the imaginary component (inductive reactance) can be cancelled by a matching capacitor C_M in series with the circuit:

$$Z_T(Imaginary) = \frac{1}{\omega.C_M} \Rightarrow C_M = \frac{1}{\omega.Z_{in}.A} \quad (4.9)$$

C_M was calculated to be 6.67 nF. When these theoretical values were applied, we measured the impedance of ~50 Ω rather 9.25 Ω across the tuning-matching circuit output (V_{TMI}). There are multiple possible reasons for this: the switch and the output amplifier impedance is not purely resistive. Coaxial cables also have a characteristic impedance of 50 Ω. The coil inductance and resistance may not be precisely accurate.

In practice, the capacitors values were determined using a fix capacitor for C_T and a variable capacitor for C_M within the range of 1 pF – 100 nF. C_T was set to different values in 50 pF increments, and C_M was varied until the closest impedance to 10 Ω was achieved. A signal generator (HP, Hewlett. Packard 8656B- 0.1 to 990 MHz) was applied for the power amplifier input. The signal generator output was set to 1 V and the power amplifier gain was kept constant at Av ≈ 1.8. The impedance was measured by monitoring the voltage across the tuning-matching circuit (V_{TMI}) and the current through a shunt resistor (0.25Ω, 2W) in series with C_M. The most optimum impedance was found 12 Ω when C_T = 3.25 nF and C_M = 16.9 nF. V_{TMI} and V_{TIN} signals were recorded, and the result is shown in Figure 4.6. A 25 mV DC voltage was measured on V_{TMI}. The reason for this is found to be in on-resistance (1.25Ω) of the analog switch. During transmission, the switch-1 is "on" (closed) and the switch-2 is "off" (open) (Fig. 4.5). The transmit signal, thus, is dropped by the DC voltage across on-resistance of the switch-1. During receive, the switch-1 is "off" and the switch-2 is "on". Therefore, C_T and C_M are discharged through on-resistance of the switch-2. The DC signal is rolled off when it passes through C_M. Thus, a pure AC signal can be seen across the transmit coils.

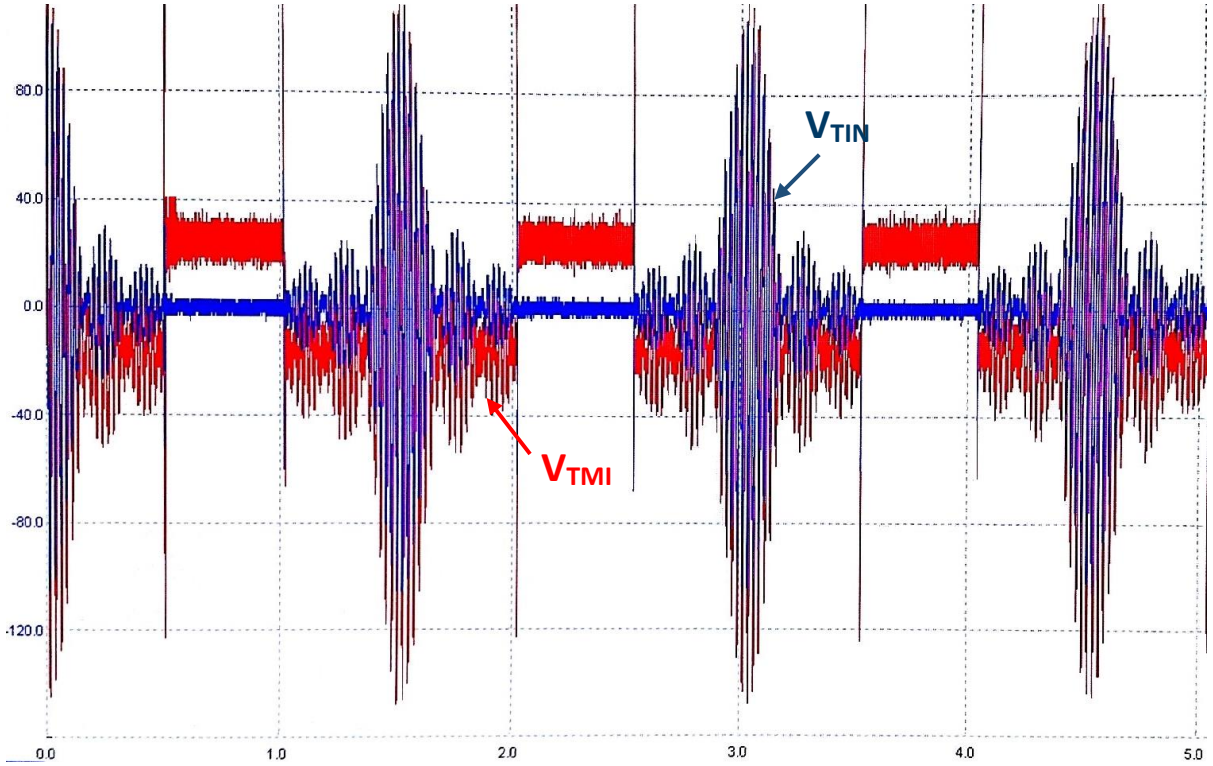

Figure 4.6. V_{TMI} in red and V_{TIN} in blue. The DC voltage measured on V_{TMI} is rolled off by passing through tuning and matching circuit.

***Transmit signal calibration*:** To calibrate the transmit pulse, the configuration shown in Figure 4.4 was considered. The power amplifier gain was kept constant at Av ≈ 1.8, and the pulse time was set to 1 ms. "ENABLE_TX" input parameter of the Matlab program was set to 1 to enable transmit channel of the radioprocessor board. Pulse amplitude of the transmit signal was first set to 0.01 (arbitrary unit), and then increased in 0.04 increments for the next trials. Voltage was measured across the board output channel (V_{TO}), the power amplifier output (V_{PO}) and transmit coils (V_{TIN}). These points are shown in Figure 4.4. The results were recorded and are shown in Table 4.3. According to the observed data, a pulse amplitude of 0.48 (arbitrary unit) on the acquisition card generates 5 V across the transmit coils which corresponds to a 90-degree flip angle. These measurements were carefully performed, as there was a concern that the transmit-receive switch could be damaged from overcurrent. The switch has a peak continuous current limit of 200 mA and 1ms pulsed current of 300 mA. Since the measured impedance across tuning-matching circuit is 12 Ω, the maximum level for the pulse amplitude must not exceed 0.61. The expected current through the switch for a 1ms 90° pulse is ~178 mA.

No.	Transmit Pulse Amplitude (arbitrary unit)	V_{TO} (mV)	V_{PO} (mV)	V_{TIN} (V)
1	0.01	25	45.5	0.12
2	0.05	115.75	250	0.53
3	0.09	224.5	423	0.95
4	0.13	332.5	597	1.4
5	0.17	425.2	765	1.84
6	0.21	519.5	934	2.26
7	0.25	624	1097	2.67
8	0.29	734	1261	3.07
9	0.33	837	1436	3.48
10	0.37	940	1611	3.9
11	0.41	1044	1789	4.32
12	0.45	1147	1964	4.74
13	0.49	1250	2139	5.16
14	0.53	1355	2314	5.58
15	0.57	1459	2489	6.01
16	0.61	1564	2664	6.43

Table 4.3. Transmit signal calibration based on amplifier gain of Av = 1.8, and pulse time of 1 ms. The row colored in green shows the most optimum value for a 1ms, 90-degree pulse, and the red row shows the limit that should not be exceeded for the safety of the transmit-receive switch. V_{TO}, V_{PO} and V_{TIN} points are shown in Figure 4.4.

4.5 Polarisation Calculation

The nuclear magnetization from the xenon nucleus is found according to equation 2.5. This equation can be expressed in the unit of nuclear magneton μ_N = 5.05078353 × 10^{-27} J/T:

$$\vec{\mu} = -0.778\,\mu_N \tag{4.10}$$

The maximum bulk magnetization is found by adding up the component of the nuclear magnetic moment of each spin on this direction:

$$\vec{\mu} = -0.778\,\mu_N.N \tag{4.11}$$

where N is the number of xenon atoms present in the SEOP cell at the room temperature and partial pressure of xenon. The induced magnetic field resulting from this magnetization is:

$$\vec{B}_i = \mu_0.\vec{\mu}\,.P\% \tag{4.12}$$

Where P% is the polarisation degree.

The number of xenon atoms can be calculated based on the ideal gas law:

$$N_{Xe} = \frac{P_{Xe}.V}{K_B.T_{Xe}}.\beta_{129} \tag{4.13}$$

where P_{Xe} is xenon partial pressure in the gas mixture, V is volume of the SEOP cell, K_B is Boltzmann constant, T_{Xe} is the xenon gas temperature, and β_{129} is the xenon enrichment factor. Xenon was provided with 99.985% isotopically enriched from ISOFLEX USA. SEOP glass cell volume is 270.21 ml of which 5% volume fraction contains xenon in room temperature and 1 atm pressure. Therefore, the number of xenon nuclei present in the cell is N ~ 5 × 10^{11} m^{-3}. Thus, the induced magnetic field

by Xe is B_i = 1.23 nT for 50% polarisation. The field calculated for different polarisation degrees is shown in Figure 4.7.

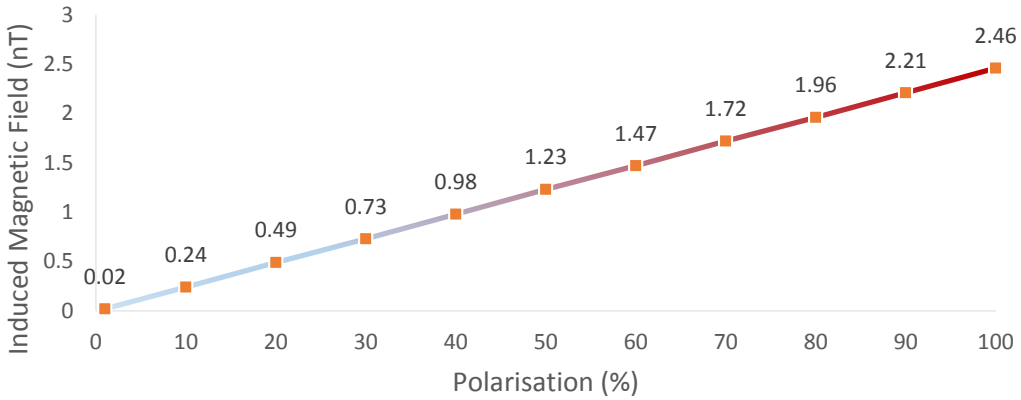

Figure 4.7. Corresponding induced magnetization within the receive coils to the polarisation degree

4.6 Receive Path

Receive path was discussed in Sections 3.5.3 and 3.5.4. The components with their input and output impedances are shown in Figure 4.8. Calibration and measurement results are discussed in three sections in detail: impedance matching, receive signal calibration and noise characterization:

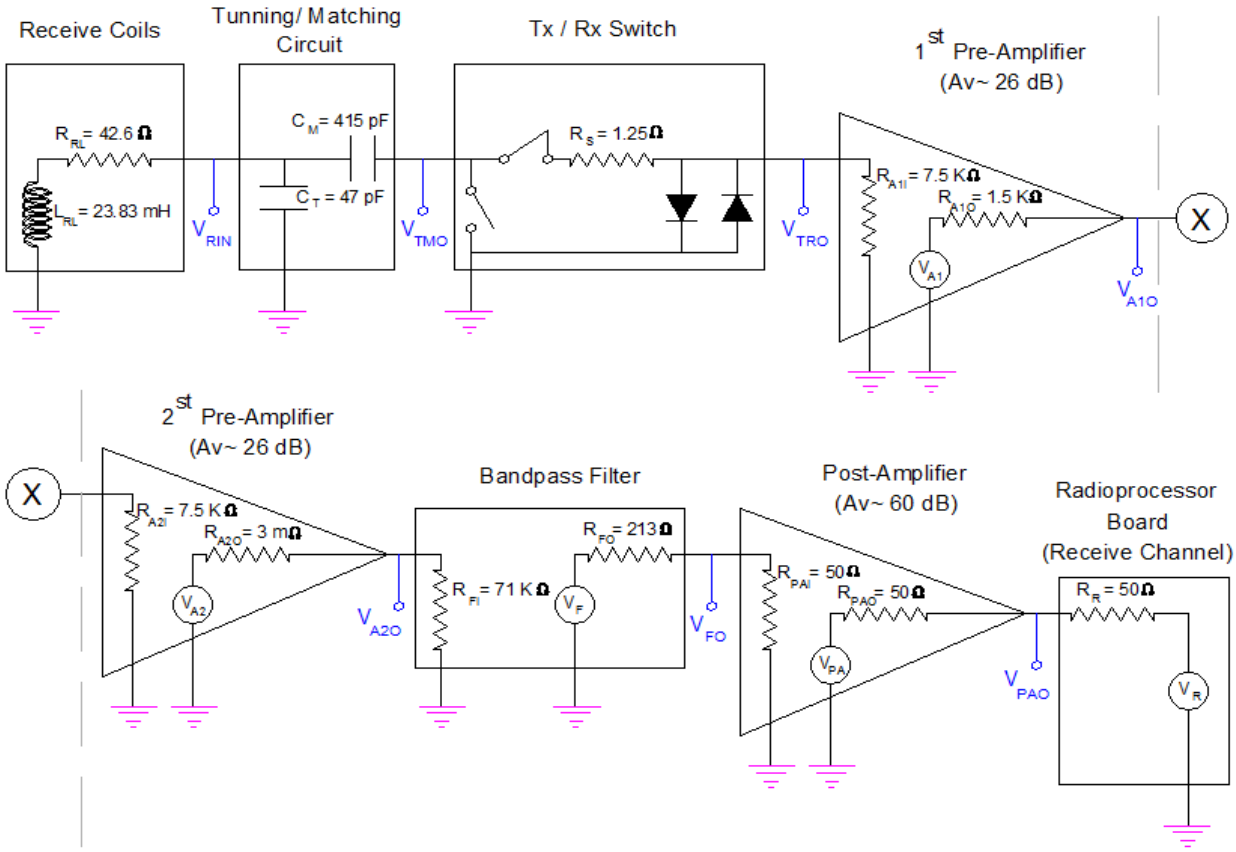

Figure 4.8. Receive path electronic equipment with their input-output impedances

Impedance matching: Receive coils must resonate at the frequency corresponding to the Larmor frequency of xenon nuclei at 3.56 mT. Thus, a tuning-matching circuit, with two capacitors C_T and C_M, is used to adjust the resonance frequency to 42 kHz. To measure C_T and C_M values, a single loop coil (Diameter = 15 mm) was driven by the signal generator to simulate the polarisation from xenon nuclei. The loop coil was positioned between two receive coils so that its magnetic field axis was in parallel with the receive coil axis. The output signal was viewed on a digital Picoscope across a 7.5 kΩ which resembles the input impedance of the first pre-amplifier. This configuration is shown in Figure 4.9. A fix capacitor for C_T and a variable capacitor for C_M (1 pF – 100 nF) were considered similar to what was done for tuning-matching of the transmit coils. Signal generator was set to 200 mV with different frequencies. C_T was set to different values in 50 pF increments, and C_M was varied until the highest signal amplitude was achieved at 42 kHz. C_T = 47 pF and C_M = 415 pF were found as the most optimum values. Impedance at the point V_{TMO} was measured to be 3.3 kΩ by monitoring voltage at this point and current through a shunt resistor (0.25Ω, 2W) in series with C_M.

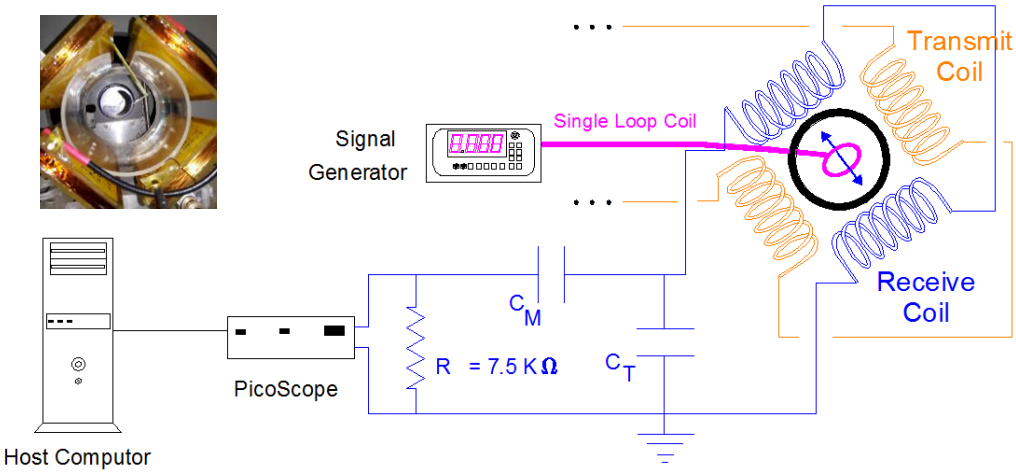

Figure 4.9. Tuning-matching of receive coils using a small loop coil driven by a signal generator. 7.5 kΩ resembles the input impedance of the first pre-amplifier. The image on the top left shows the position of the loop coil in regards with the receive coils.

Input impedance of other components in receive path were measured by monitoring the voltage across a shunt resistor in series with the input, and the current through the shunt resistor. To find the output impedance, the output voltage is measured first with no load resistor, then with a fixed known resistor. The output impedance can be calculated by the voltage division rule. Having input and output impedances of all components, we were able to determine the best succession of components in order to have the most optimum SNR at the input channel of the radioprocessor board.

Receive Signal Calibration: The induced current into the receive coil by the small coil was amplified ~12,000 times after passing through the receive path components and was eventually reached to the input channel of the radioprocessor board. "ENABLE_TX" and "ENABLE_RX" input parameters of the Matlab program were set to 0 and 1 respectively to disable the transmit channel and enable the

receive channel to acquire data. The acquired data and its frequency profile was plotted using Matlab. A software low-pass filter was written to suppress undesired high frequencies. The amplitude of the signal was recorded, and the corresponding SNR was measured. The corresponding polarisation level was estimated based on the field at the centre of the small coil and diagram 4.7. The minimum polarisation level that can be measured by receive electronics is 10%. Received signals corresponding with polarisation levels of 10% and 90% are shown in Figure 4.10.

The Hall sensor has the sensitivity of 25 mV/Gauss as mentioned before. Thus, it can only detect field changes above 0.1 mT while the induced magnetization is in the range of nT. However, the sensor performance is linear offering the advantage of measuring the field for higher voltages across the loop coil (>80 mV) and estimating it for much less values (< 1 mV).

Field at the Centre of the Small Coil	Voltage Across RF Board Input Channel (V_{PAO})	(FID) Signal Amplitude	SNR	Polarisation Degree
nT	**mV**	**-**	**-**	**%**
0.23	33.8	0.95E+06	1	10
0.46	66.2	3.11E+06	3	21
0.69	92.5	5.93E+06	6	30
0.92	118.3	8.04E+6	8	41
1.15	160	1.56E+07	15	54
1.38	181.8	2.81E+07	28	65
1.61	208.3	3.93E+07	39	75
1.84	223.8	5.04E+7	50	85
2.07	234.3	6.77E+07	67	96
2.3	322.6	7.73E+07	77	100

Table 4.4. Receive signal calibration. The loop coil was applied to simulate the polarisation from xenon nuclei. The field on its centre resembles magnetization from xenon nuclei (first column), and induces a current through the receive coils. The signal was received on input channel of radioprocessor board after 12,000 amplification (second column). The signal amplitude captured by the board, its corresponding SNR and calculated polarisation levels are shown in three last columns.

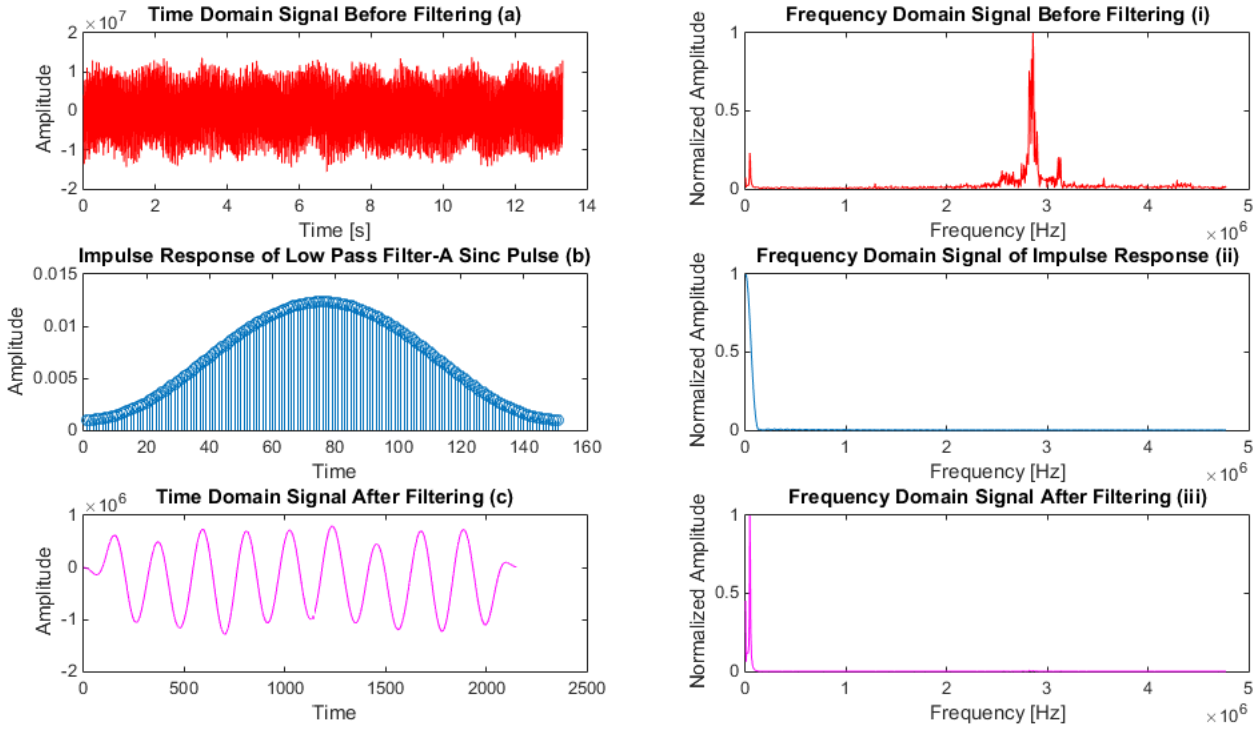

(a)

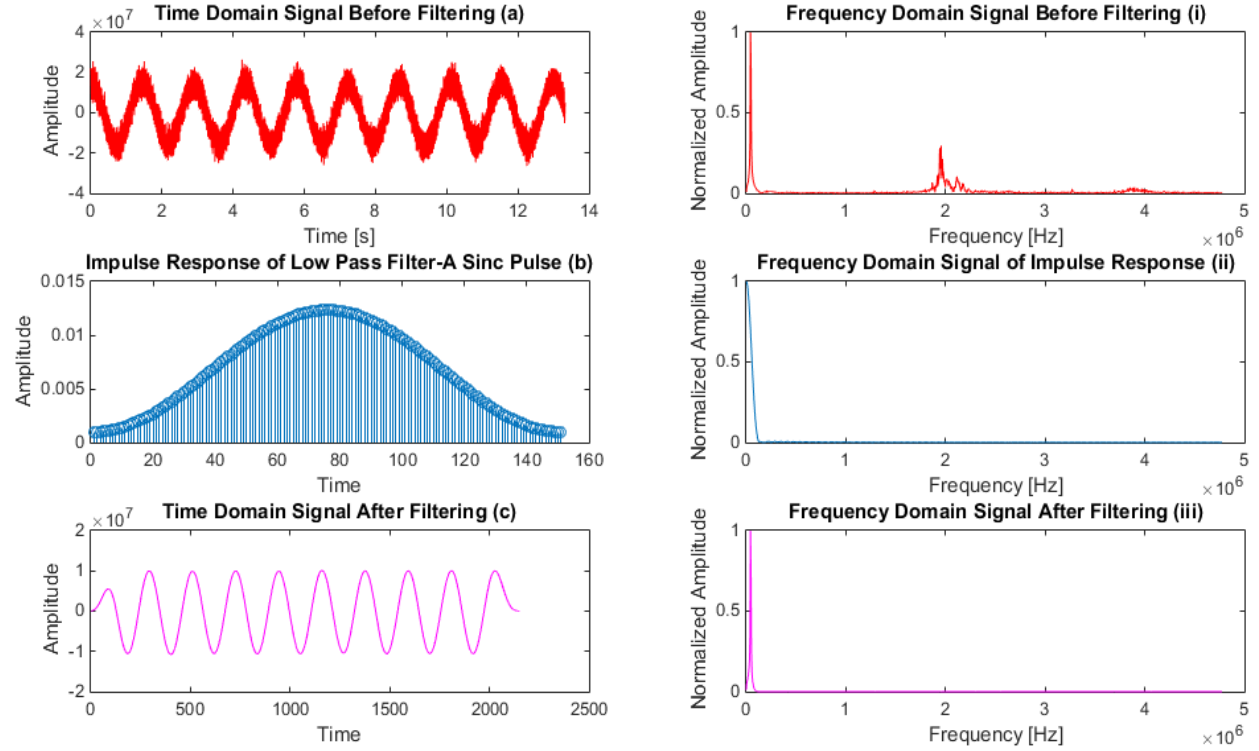

(b)

Figure 4.10. Acquired signals by radioprosessor board shown in Table 4.4 (third column) for 10% (a) and 50% (b) polarisation are plotted. The main receive signals are shown in the first rows with their corresponding frequency profiles. A software low pass filter was developed to suppress high frequencies from the signal. Impulse response of the filter is shown in second rows while the filtered signals are presented on the third rows.

***Noise characterization*:** Driving the small loop coil by 600 µV corresponds to 1 nT magnetization from xenon nuclei and 50% polarisation. 1 nT magnetization can only create the voltage of 10 µV across the input of the first pre-amplifier. Since the induced signal is very small, the noise present in the electronics can override and wash out any signal that is present. Tests were therefore conducted to characterize the noise beginning with only the coil and tuning-matching circuit while other receive components were systematically added. Table 4.5 shows the progression of noise as each electronics were added to the receive path.

Point	Equipment On	Noise Amplitude (mV)
V_{TMO}	Receive coil, Tuning-Matching Circuit	5
V_{TRO}	Receive coil, Tuning-Matching Circuit, Transmit-Receive Switch	25
V_{A2O}	Receive coil, Tuning-Matching Circuit, Transmit-Receive Switch, Two Pre-amplifiers	80
V_{FO}	Receive coil, Tuning-Matching Circuit, Transmit-Receive Switch, Two Pre-amplifiers, Band pass filter	5
V_{PO}	Receive coil, Tuning-Matching Circuit, Transmit-Receive Switch, Two Pre-amplifiers, Band pass filter, Post-amplifier	Unable to measure by Picoscope
V_R	Receive coil, Tuning-Matching Circuit, Transmit-Receive Switch, Two Pre-amplifiers, Band pass filter, Post-amplifier, Radioprocessor Board	-

Table 4.5. Experimental setup used for noise characterization in the receive path. Noise level arising from each stage of the receive path was measured. V_{TMO}, V_{TRO}, V_{A2O}, V_{FO} and V_{PO} points are shown on Figure 4.8. V_R is the signal captured by the radioprocessor board.

The first trial was done while receive coils with tuning-matching circuit were connected to a 7.5 kΩ resistor corresponding to the next stage input impedance. The small loop coil was driven by the signal generator. The supply voltage on signal generator was set large enough to allow measurement of the signal across 7.5 kΩ resistor by Picoscope. The signal was detected across the resistor with a high SNR level showing the well-tuned and well-matched design of the receive coil with tuning-matching circuit. 5 mV noise measured on the signal is mainly because of the Picoscope which has a 2 pF capacitor and 2 MΩ resistor probe with ground alligator clip connector. For the second trial, the transmit-receive switch was added and 7.5 kΩ resistor was connected to its output. The switch introduces 20 mV more noise level to the first trial. The noise is mostly dominated by high frequencies resulted from a dual supply operation of the switch (±15 VDC and 5 VDC). The third trial was conducted while two pre-amplifiers were added. Noise level was increased to 80 mV. The noise created from the first pre-amplifier is amplified and introduced to the second one. Pre-amplifiers are supplied by ±15 VDC power supply which is the main source of noise. By adding band pass filter on the forth trial, the noise level back to 5 mV on the first trial. The post-amplifier was added after the band pass filter since its 50 Ω output impedance matches with 50 Ω input impedance of the receive

channel of radioprocessor board. Measuring voltage across the output of post-amplifier was not possible by picoscope due to saturation of the 2 pF internal capacitor of the picoscope probe. The radioprocessor board was added as the last stage. Supply across the loop coil was decreased to the voltage corresponding to the polarisation degree of xenon nuclei from 1% to 100% and the noise level was characterized. Below 10% of polarisation, noise overrides the signal. By increasing the polarisation degree, SNR also increased up to the level of 50 for higher polarisation degrees.

4.7 Temperature Calibration

The SEOP cell is heated up to 150– 160 °C by use of a heating wire to vaporise Rubidium droplet sitting inside the cell. The homebuilt J-type thermocouple monitors temperature inside the cell. The thermocouple was connected to the gas-flow acquisition card via an interface circuit. A Matlab program was developed to operate the thermocouple. To calibrate the thermocouple, a simple calibration process was conducted. It was immersed in boiling water of which the temperature was monitored using a thermometer. The Matlab program was run, and the data corresponding to water temperature was recorded. For temperatures above 100 °C, the data was estimated since thermocouple performance is linear. The calibration setup and a view from the plotted data on Matlab program are shown in Figure 4.11. The acquired data was averaged for each temperature and is presented in a plot in Figure 4.12.

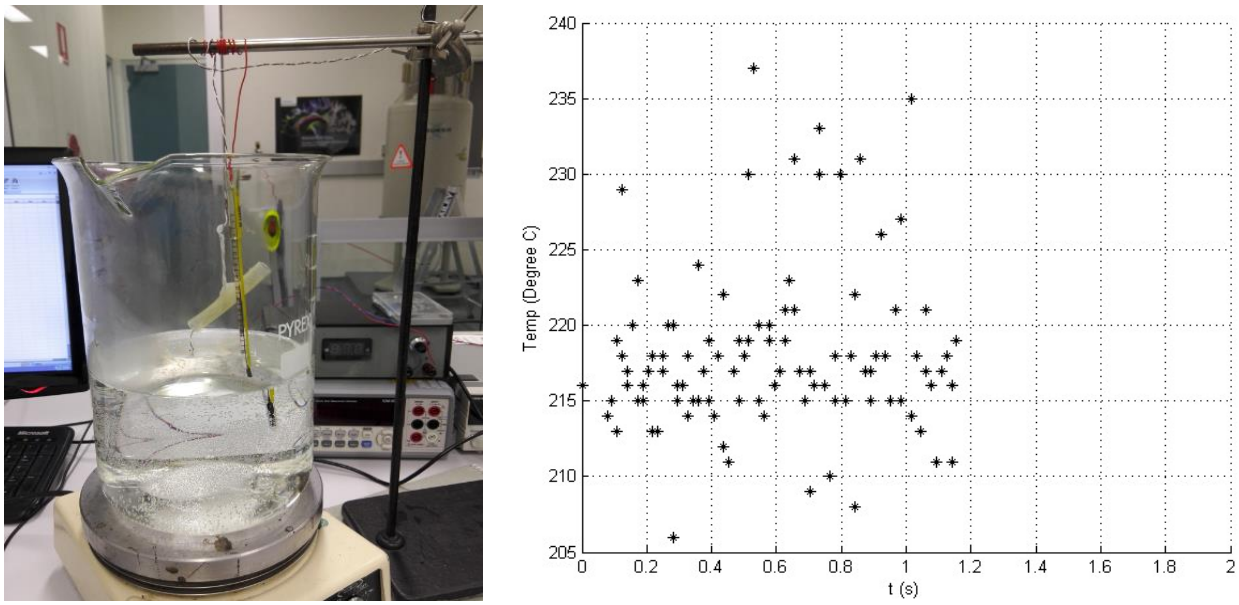

(a) **(b)**

Figure 4.11. Setup for temperature calibration (a) includes boiling water, a thermometer and the thermocouple. Thermocouple transmits the data to an acquisition card via an interface board. The acquired data by the acquisition card is plotted in the Matlab program (b). The plot corresponds to 22°C.

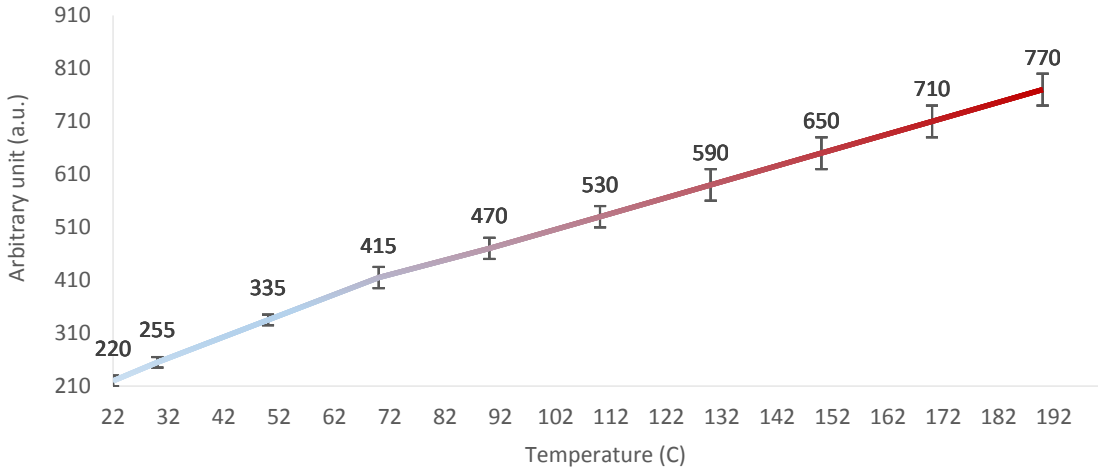

Figure 4.12. Thermocouple calibration. The solid line relates to the average values for the data plotted in Figure 4.11(b) for each temperature. The vertical error bars represent the maximum and minimum measured values (90 measurements per data points) for each set temperature.

The warm-up time to achieve 150 °C in the SEOP cell was measured to be 45 minutes. For having this time span, the DC power supply must set to 10.7 V which generates about 2.39 A through the heating wire.

4.8 Laser Tuning and Characterization

Laser is the transferring source of angular momentum to the rubidium valence electron in optical pumping process. Its wavelength needs to be tuned to the rubidium D1 absorption line of 794.7 nm. Our laser has a central wavelength between 794.4 and 795.4 nm with FWHM of 0.3 nm. Operating the laser at different current and different base temperature affects the central wavelength. The current can be set from 0 to 50 A and the base temperature can be increased from 10°C to 50°C from the WinVue 4.011 HCT user interface. Wavelength spectrum is recorded by use of Ocean Optics SpectraSuite software. The relationship between base temperature and operating current with laser wavelength was characterized as follows:

The laser base temperature was set to room temperature, 22 °C, and was allowed to equilibrate. Setting base temperature lower than room temperature can endanger laser diode arrays' emitters surface by condensation of water vapour from the air. The laser current was then increased in 2 A increments. After each increment, the laser wavelength and base temperature were both allowed to equilibrate. The wavelength, then, was recorded. This process was repeated for increments of 1 °C for base temperature until the most optimum parameters were achieved. The result is shown in Table 4.6.

Laser Base Temperature (°C)	Central Wavelength (nm)
22	Major peak @ 790 nm (Current 0:12 A)
23	Major peak @ 791 nm (Current 0:12 A)
24	Two major peaks @ 791 nm and 794.5 nm (Current 0:12 A)
25	Two major peaks @ 791 nm and 794.5 nm (Current 0:12 A)
26	**@ Current 10.2 A: only one peak @ 794.7 nm** @ Higher currents: one @ 794.7 nm and one @ 791 nm
27	Two major peaks @ 794.7 nm and 791.1 nm (Current 0:12 A)

Table 4.6. Laser wavelength measurements at different base temperatures and different currents. The data indicates that our Laser gives stable wavelength of 794.7 nm at 10.2 A and 26 °C.

4.9 Operational Protocol of the Polariser

To operate the polariser a "protocol" was developed. The protocol is presented in two main sections: Preparation of the SEOP setup and Preparation of the NMR setup. It is assumed that everything is already connected.

Preparation of the SEOP setup: The SEOP glass cell must be loaded with Rubidium. This process requires precaution since Rb is highly reactive. It reacts very rapidly with water, ignites easily in contact with air, and becomes oxidized in the presence of oxygen. Rb oxidization consists of three main phases depending on the amount of oxygen to which Rb is exposed. Sub-oxides such as Rb_9O_2 and Rb_6O are formed in the first phase (Fig.4.13a). They have a copper color. Yellowish-colored oxides such as rubidium oxide (Rb_2O) and rubidium peroxide (Rb_2O_2) occur in the second phase (Fig.4.13b). The third phase is superoxide (RbO_2) which has a dark brown color.

(a) **(b)**

Figure 4.13. Rubidium oxidation. rubidium suboxide (a) and rubidium oxide (b)

Cleaning the cell from Rb oxide: If the cell has previously been used, it is contaminated with a layer of Rb and Rb oxide. To refill the cell with fresh Rb, thus, it needs to be taken apart and cleaned. Close the inlet glass stopcock, and separate it from the twin vacuum-gas adapter. Transport the cell to a

chemical hood while the stopcock is still attached. Slightly open the stopcock and the screw cap on two side wings of the cell. This allows a small amount of air to permeate into the cell. Leave the cell under the hood overnight. When yellowish color of Rb oxide is appeared, completely open the glass cell on its two side wings and wait for 2 hours. Rubidium oxide reacts slowly with humidity in air resulting in the formation of colorless rubidium hydroxide (RbOH) droplets. Flush the cell with nitrogen through one of side wings. At the same time, pipette pure acetone into the cell and gently shake it. Continue with pipetting acetone until there is no further Rb puddle remained. Thereafter, add some water. When Rb reacts with water, large amount of hydrogen is produced. Thus, flushing the cell with nitrogen is essential. A normal cleaning can be done with acetone once all Rb disappears.

Refilling the cell with fresh Rb: Transport the cell to a nitrogen glovebox with the stopcock and the screw cap to which the thermocouple and the board interface are attached. Also include a Rb ampoule, a tool for breaking the ampoule, a clamp attached to a retort stand to hold the Rb ampoule, a Pasture pipette, a heat gun, and a glass container to put the remained Rb inside. To monitor the presence of oxygen into the glovebox, a portable oxygen-meter (WTW, Oxi-325) can be applied. Open the glovebox inlet valve, and monitor O_2 level. Once O_2 density reaches 2.5 mg/l, conditions are fine to expose Rb to the glovebox atmosphere. Break the Rb ampule, and clamp it to the retort stand. Melt Rb by the heat gun, soak up some Rb by the use of pipette and inject it into the glass cell. Place the ampoule into the glass container ensuring that the container is completely sealed. Flush the cell with nitrogen before being closed from its two side wings. Take the cell with its accessories out of the glovebox to be reinstalled into the polariser. Connect the stopcock to the twin vacuum-gas adapter. Connect the interface board of the thermocouple to the USB interface card (Velleman, K8061), and check the connection to be established.

Evacuating the gas-vapour flow system: Evacuate the mixing vessel up to the outlet flowmeter by opening the manual and the proportional solenoid vacuum valves related to the forth tapper of the vessel. After having the minimum achievable pressure of 7×10^{-4} atm, fill the lines and the mixing vessel with N_2. Repeat this for twice, evacuate the vessel afterwards from N_2. Open the xenon flow controller valve for 5 seconds to elliminate oxygen impurities in its line. Then, fill the vessel with ^{4}He. Open the manual vacuum valve connected to the twin vacuum-gas adapter to pull vacuum through the outlet line. At the same time, open the exhaust proportional solenoid valve allowing helium to flow through the delivery line. After two minutes, open the stopcock on the pumping cell. The cell is pulled vacuum. Close the vacuum valve on the twin vacuum-gas adapter. Evacuate the vessel from the remained helium. Close both vacuum valves in the vacuum line.

Gas mixture preparation: To refill the mixing vessel with a gas mixture of 85% Helium, 10% Nitrogen and 5% xenon, first partially open the helium flow controller valve (70% opening position) for 740 second. The pressure increases from the minimum 7×10^{-4} atm to 0.85 atm. The nitrogen valve must then partially be opened (50% opening) for 120 seconds. Pressure increases to 0.96 atm. Open the xenon control valve with 50% opening for 53 seconds. This increases pressure inside the cell to 1 atm. Open the proportional valve in the delivery line to the cell for 5 seconds. The cell is loaded with the gas mixture.

Heating the SEOP cell: To vaporise Rb the cell needs to be heated up. Turn on the DC power supply of the heating wire (Tenma, 72-10480). Set the voltage to 10.7 V. Monitor the temperature inside the cell by running the corresponding Matlab program. The estimated time for reaching temperature to 150 - 160°C is 45 minutes. Once the temperature reaches this point, it is fixed manually by continually turning on-and off the power supply.

Tuning the laser to wavelength 794.7 nm: Ensure that all three interlocks are closed, and nothing unwanted is in the beam path. Turn on the power meter, the spectrometer and the camera. Run their related user interfaces. Turn on the laser power and run its user interface (WinVue 4.11 HCT). Enable the servo and set temperature to 26 °C in 2 degrees' increments. After each increment, allow the temperature to equilibrate. Put on the laser safety goggles. Turn on the laser, and set the current to 10.2 A in 2 A increments. After each increment, allow the servo temperature to equilibrate. Monitor the laser profile through the spectrometer assuring that centre wavelength is tuned at 794.7 nm. If a sufficient quantity of Rb vapour is present in the cell, the laser light will be absorbed by Rb, thus the laser spectral peak will be attenuated. Turn on the B_0 coils while monitoring the laser profile. Transmission should go up immediately as the field causes selective optical pumping. Ensure that the power supply of the field B_0 set to 6 A. The polariser is now ready to use.

Preparation of the NMR Setup: The input parameters of the Matlab program to control transmit-receive process should be set as follow:

To determine the required excitation pulse time, refer to Table 4.1. Assuming a $\frac{\pi}{2}$ RF pulse within a "PULSE_TIME" of 1 ms, the required voltage across the transmit coils to excite the xenon nuclei for 90 degrees is ~5 V. Thus, according to Table 4.3, setting the pulse "AMPLITUDE" to 0.48 (arbitrary unit) will generate 5 V across the coils. Other parameters are: BOARD_NUMBER: **0**; ADC_FREQUENCY: **75 kHz**; ENABLE_TX: **1**; ENABLE_RX: **1**; REPETITION_DELAY: **as required**; NUMBER_OF_SCANS: **as required**; NUMBER_OF_POINTS: **as required**; SPECTROMETER_ FREQUENCY: **42 kHz**; SPECTRAL_WIDTH: **as required**; TRANS_TIME:

as required; TX_PHASE: **0**; SHAPED_PULSE: **1**; BYPASS_FIR: **0**; FNAME: **as desired**; VERBOSE: **1**; BLANKING_EN: **1**; BLANKING_BIT: **2**; BLANKING_DELAY: **as required.**

Run the Matlab Program, and acquire the signal. Measure the peak amplitude of the FID signal in the spectrum. The signal intensity for the hyperpolarised xenon gas mixture identify the polarisation degree which is presented in Table 4.4.

This “protocol” was implemented on the system for twice to achieve xenon polarisation. However, Rb became oxidized during operation probably because of air permeation from joints and silicon tubes during vacuum. Since, the required setup for SEOP and gas-vapour flow system, laser and optics system, NMR hardware, heating apparatus and the operational protocol are all provided, quantizing leakage by a recently added oxygen sensor will help us to address the only issue remained in the system to have the polarisation result.

5

Conclusions and Future Work

5.1 Conclusion

The hyperpolarised gas generator is currently under construction at Macquarie University. The design has undergone much progress over time as a better understanding with its components has been achieved. Improvements in hardware were achieved on the NMR unit and the gas-vapour flow system. NMR transmit circuit were optimized through impedance matching of its components. The NMR receive path underwent a new design to detect polarisation as low as 10%. The noise characteristics of the receive channel were analyzed. Hardware and software filters were applied to attain a SNR as high as 50 for higher polarisation degrees. A new efficient active switching circuit was designed to prevent the residues of the transmitted signal leaking into the receiver circuitry.

A new design was implemented on the SEOP cell to prevent Rb from contaminating with air during operation and transportation from the nitrogen glovebox to the polariser. Leakage from the gas-vapour flow system was substantially reduced. We decided to run the polariser at a pressure close to atmosphere. A lower value will allow the air to rush in from the joints, a higher value will make the joints in tubing unsafe. However, it was found that Rubidium still becomes oxidized during operation. Air permeating through joints and silicon tubes during vacuum are the possible reasons. The system was recently equipped with an oxygen sensor to quantify the leakage. A gas purifier may be added to the unit after measuring the amount of the leakage.

In addition, precise calibrations were done through repetitive measurements to find the optimum parameters of the polariser. NMR transmit signal was calibrated to excite xenon nuclei at identified flip angles. New methods were developed to calibrate the receive signal in regards with the polarisation degree. The Laser beam was characterized by tuning the laser current and the base cooling temperature. We developed a protocol for operating the polariser with its optimized parameters. A Matlab program was also further developed to control transmit-receive NMR process using a source code (in C-language) proposed by the radioprocessor board manufacturer.

5.2 Future Work

Five major phases are defined for the current project as described in Section 1.4. The work described in this thesis is defined to satisfy the first phase of the project through the preparation of hyperpolarised ^{129}Xe gas on a small scale polariser. There are still some issues remained in the system. Polarisation under 10% cannot be detected by the present receive path electronics. Adding another pre-amplifier and a low pass filter to the receive path will help in improving the receive signal. Oxygen leakage must be eliminated probably by adding a gas purifier on the inlet of the SEOP cell. Once hyperpolarisation is achieved, an accumulation and extraction unit will be developed. A transportation method for the polarised xenon must also be designed.

Further improvements are planned. The system will be upgraded to a fully computer controlled polariser. The upgrade will be implemented on both the gas-vapour flow system and the NMR setup. A Matlab graphical user interface (GUI) will be developed to monitor and control pressures, flow rates and temperature. Another Matlab GUI interface will be designed for the NMR setup to run NMR experiments with ease. The GUIs will have two substantial advantages: Firstly, they allow quick and easy interaction with the system through setting experimental parameters and previewing data immediately after the scan. Secondly, a better understanding of the polarisation dependencies on each parameter can be achieved. These advantages will reflect on improvements in polarisation degree.

When a sufficient amount of polarisation is achieved, preclinical MRI experiments will be performed at the preclinical MRI facility of the University of New South Wales (UNSW) as the second phase (post-MRES). These experiments will focus on functional lung imaging in phantom and small animals. In the third phase of the project, large-scale continuous-flow hyperpolarised gas polariser, currently under construction, will be further developed and optimized. This system will be able to polarise larger volume of gas with a sufficient degree of polarisation for human lung imaging in the fourth phase. In the fifth phase, further research will also focus on using hp-^{129}Xe for molecular imaging.

References

[1] Albert MS, Cates GD, Driehuys B, et al. *Biological magnetic resonance imaging using laserpolarised ^{129}Xe*. Nature. 1994; 370(6486):199–201.

[2] Mugler JP 3rd, Driehuys B, Brookeman JR, et al. *MR imaging and spectroscopy using hyperpolarised ^{129}Xe gas: preliminary human results*. Magn Reson Med. 1997; 37(6):809–815.

[3] Mugler, J.P. and T.A. Altes, *Hyperpolarised ^{129}Xe MRI of the human lung*. Journal of Magnetic Resonance Imaging, 2013. 37: p. 313-31.

[4] MacDonald A, Wann K. *Physiological Aspects of Anaesthetics and Inert Gases*. London: Academic Press; 1978.

[5] Walker TG, Happer W. *Spin-exchange optical pumping of noble-gas nuclei*. Reviews of Modern Physics. 1997; 69:629–42.

[6] Zhang, G., et al., *Functional lung imaging in thoracic cancer radiotherapy*. Cancer Control, 2008. 15(2): p. 112.

[7] Sukstanskii, A. and D. Yablonskiy, *In vivo lung morphometry with hyperpolarised ^{3}He diffusion MRI: Theoretical background*. Journal of Magnetic Resonance, 2008. 190(2): p. 200-210.

[8] Wild, J.M., N. Woodhouse, and K. Teh, *Single-scan acquisition of registered hyperpolarised ^{3}He ventilation and ADC images using a hybrid 2D gradient-echo sequence*. Magnetic Resonance in Medicine, 2007. 57(6): p. 1185-9.

[9] Deninger, A.J., et al., *Quantification of Regional Intrapulmonary Oxygen Partial Pressure Evolution during Apnea by 3He MRI.* Journal of Magnetic Resonance, 1999. 141(2): p. 207-16.

[10] Gast, K.K., et al., *Two-dimensional and three-dimensional oxygen mapping by ^{3}He-MRI validation in a lung phantom*. European radiology, 2005. 15(9): p. 1915-22.

[11] Yu, J., et al., *Optimization of scan parameters in pulmonary partial pressure oxygen measurement by hyperpolarised ^{3}He MRI*. Magnetic Resonance in Medicine, 2008. 59(1): p. 124-31.

[12] Ruppert, K., et al., *Exploring lung function with hyperpolarised ^{129}Xe nuclear magnetic resonance*. Magnetic resonance in medicine, 2004. 51(4): p. 676-87.

[13] Spence, M.M., et al., *Functionalized xenon as a biosensor. Proceedings of the National Academy of Sciences*, 2001. 98(19): p. 10654-7.

[14] Imai, H., et al., *Hyperpolarised ^{129}Xe lung MRI in spontaneously breathing mice with respiratory gated fast imaging and its application to pulmonary functional imaging*. NMR in Biomedicine, 2011. 24(10): p. 1343-1352.

[15] Altes, TA.; Mugler, JP.; Dregely, IM., et al. *Hyperpolarised xenon-129 ventilation MRI: preliminary results in normal subjects and patients with lung disease (abstract)*. Proceedings of the 18th Annual Meeting of ISMRM; Stockholm. 2010. p. 2529.

[16] Altes, TA.; Mugler, JP.; Meyer, C., et al. *A comparison of hyperpolarised helium-3 and xenon-129 MR ventilation imaging in cystic fibrosis (abstract)*. Proceedings of the 20th Annual Meeting of ISMRM; Melbourne, Australia. 2012. p. 1354.

[17] Ewald R. Weibel, *It Takes More than Cells to Make a Good Lung*, Occasional Essay, Am J Respir Crit Care Med Vol 187, Iss. 4, pp 344, Feb 15, 2013.

[18] Saam B, et al. *relaxation of He-3 in the presence of O_2*. Physical Review A. 1995; 52(1): 862-5.

[19] Miller GW, et al. *A short-breath-hold technique for lung pO_2 mapping with ^{3}He MRI.* Mag Res Med. 2010; 63(1): 127-36.

[20] Deninger AJ, et al. *Quantification of Regional Intrapulmonary O_2 Partial Press. Evolution during Apnea by ^{3}He MRI.* Mag Res Med. 1999; 141:207-16.

[21] Phelps, M.E., PET: *a biological imaging technique. Neurochemical research*, 1991. 16(9): p. 929-40.

[22] Aime, S., et al., *Pushing the sensitivity envelope of lanthanide-based magnetic resonance imaging (MRI) contrast agents for molecular imaging applications*. Accounts of chemical research, 2009. 42(7): p. 822-31.

[23] Spence, M.M., et al., *Functionalized xenon as a biosensor.* Proceedings of the National Academy of Sciences, 2001. 98(19): p. 10654-7.

[24] Walker, T.G. and W. Happer, *Spin-exchange optical pumping of noble-gas nuclei*. Reviews of Modern Physics, 1997. 69(2): p. 629.

[25] Swanson, S.D., et al., *Brain MRI with laser-polarised ^{129}Xe*. Magnetic resonance in medicine. 1997. 695-8.

[26] Swanson, et al., *Distribution and dynamics of laser-polarised ^{129}Xe magnetization in vivo*. 1999.

[27] Nikolaou, et al., *Multidimensional Mapping of Spin-Exchange Optical Pumping in Clinical-Scale Batch-Mode ^{129}Xe Hyperpolarisers*. The Journal of Physical Chemistry, 2014. B 118 (18): 4809-4816.

[28] N. Bhaskar, R. Frueholz, C. Klimcak, and R. Cook, Phys. Rev. B 36, 4418.1987.

[29] Driehuys B, Cates GD, Miron E, et al., *High-volume production of laser-polarised ^{129}Xe*. Appl Phys Lett. 1996; 69(12):1668–1670.

[30] B. C. Grover. *Noble-gas nmr detection through noble-gas-rubidium hyperfine contact interaction*. Phys. Rev. Lett., 40(6), 1978.

[31] Ruset IC, Ketel S, Hersman FW. *Large production system for hyperpolarised ^{129}Xe for human lung imaging studies* Phys Rev Lett. 2006.

[32] A. L. Zook and C. R. Bowers. *High capacity production of >40% spin polarised xenon-129 for nmr and mri application at the nhmfl*. Nat. High Mag. Field Lab. Reports,8(4):20-23, 2001.

[33] D. Raftery, H. Long, T. Meersmann, et al., *High field nmr of adsorbed xenon polarised by laser pumping*. Phys. Rev. Lett., 66(5):584.587, 1991.

[34] M. S. Rosen, T. E. Chupp, K. P. Coulter, R. C. Welsh, and S. D. Swanson. *Polarised xe-129 optical pumping/spin exchange and delivery system for magnetic resonance spectroscopy and imaging studies*. *Rev. Scient. Instruments*, 1999. 70(2):1546.1552.

[35] Theodore Hughes-Riley, Joseph S. Six, et al., *Cryogenics free production of hyperpolarised ^{129}Xe and ^{83}Kr for biomedical MRI applications* J Magn Reson. 2013 Dec; 237: 23–33.

[36] Nikolaou, Panayiotis, Aaron M. Coffey, et al., *Multidimensional Mapping of Spin-Exchange Optical Pumping in Clinical-Scale Batch-Mode ^{129}Xe Hyperpolarisers*. The Journal of Physical Chemistry. 2014. B 118 (18): 4809-4816.

[37] H. Imai, J. Fukutomi, A. Kimura, and H. Fujiwara. *Effect of Reduced Pressure on the Polarisation of ^{129}Xe in the Production of Hyperpolarised ^{129}Xe Gas: Development of a Simple Continuous Flow Mode Hyperpolarising System Working at Pressures as Low as 0.15 atm*. Proc. Intl. Soc. Mag. Reson. Med. 16, 2008.

[38] U. Ruth, T. Hof, J. Schmidth, D. Fick, and H. J. Jansch. *Production of nitrogen-free, hyperpolarised ^{129}xe gas*. Appl. Phys. B, 68(1):93.97, 1999.

[39] R. G. Fitzgerald, K. L. Sauer, and W. Happer. *Magnetic resonance imaging with laser-polarised ^{129}xe*. Chem. Phys. Lett., 284(1-2):87.92, 1998.

[40] J. C. Leawoods, B. T. Saam, and M. S. Conradi. *Polarisation transfer using hyperpolarised, supercritical xenon*. Chem. Phys. Lett., 327(5-6):359.364, 2000.

[41] A. L. Zook, B. B. Adhyaru, and C. R. Bowers. *High capacity production of >65% spin polarised xenon-129 for nmr spectroscopy and imaging*. J. Magn. Reson., 159:175.182, 2002.

[42] M. A. Bouchiat and J Brossel. *Relaxation of optically pumped rb atoms on paraffin-coated walls*. Phys. Rev., 147(1):41.54, 1966.

[43] T. G. Walker, W. Happer, Rev. Mod. Phys., 69, 629, 1997.

[44] R. L. de Zafra. *Optical pumping*. Am. J. Phys., 28:646.654, 1960.

[45] T. J. Killian. *Thermionic phenomena caused by vapors of rubidium and potassium*. Phys. Rev., 27(5):578.587, 1936.

[46] S. Appelt, et al., Phys Rev. A. 58, 1412, 1998.

[47] R. Benumof. *Optical pumping theory and experiments*. Am. J. Phys., 33:151.160, 1965.

[48] K. Knagge, J. Prange, D. Raftery, Chem. Phys. Lett. 397 11 (2004)

[49] S. E. Korchak, W. Kilian, L. Mitschang, Appl. Magn. Reson. 44, 65 (2013)

[50] A. Abragam, *Principles of Nuclear Magnetism*. Oxford University Press 1961.

[51] H. G. Hecht, *Magnetic Resonance Spectroscopy*, John Wiley and Sons, Inc. 1967.

[52] H. G. Hecht, *Magnetic Resonance Spectroscopy*, John Wiley and Sons, Inc. 1967.

[53] F. Bloch, Phys. Rev 70, 460, 1946.

[54] Witte, C., Kunth, M., Döpfert, J., Rossella, F., Schröder, L. *Hyperpolarised Xenon for NMR and MRI Applications*. J. Vis. Exp. e4268 10.3791/4268.